

Electron-spin-resonance study of Tl atom defects in KCl and relativistic many-body analysis of the hyperfine structure

E. Goovaerts

Physics Department, University of Antwerp (U.I.A.) B-2610 Wilrijk, Belgium

J. Andriessen

Physics Department, T.H.D., Delft, The Netherlands

S. V. Nistor

Central Institute of Physics, I.F.T.M., C.P. 5206, Bucuresti, Roumania

D. Schoemaker

Physics Department, University of Antwerp (U.I.A.), B-2610 Wilrijk, Belgium

(Received 21 November 1980)

Two thallium atom defects of tetragonal symmetry around $\langle 100 \rangle$ are produced by x irradiation above 230 K in KCl:TlCl. Their electron-spin-resonance spectra are characterized by comparable and large g shifts but quite different hyperfine parameters. A relativistic many-body calculation of the Tl^0 atom hyperfine interaction including the effect of a tetragonal crystal field permits a quantitative analysis of the spin-Hamiltonian parameters. It is found in particular that the hyperfine data of the two Tl^0 defects can be explained by assuming the presence of one or two perturbing positive charges, respectively, and a corresponding 35 and 45% delocalization of the $6p^1$ electron on the surrounding lattice. This analysis together with x-ray production, optical-excitation, and pulse-anneal data and the fact that both Tl^0 defects can only be produced at temperatures where negative-ion vacancies are mobile (>230 K) allows one to propose precise defect structures: In one defect the Tl^0 atom (on a positive-ion site) is associated with a single negative-ion vacancy in a nearest-neighbor position along $\langle 100 \rangle$; in the other one, the Tl^0 is flanked by two nearest-neighbor negative-ion vacancies along $\langle 100 \rangle$. The data also provide strong evidence for the existence of a defect consisting of a Tl^+ ion and a nearest-neighbor anion vacancy.

I. INTRODUCTION

The $Tl^+(6s^2)$ ion is one of a series of ns^2 ($n = 4, 5, 6$) ions which when incorporated in an alkali halide crystal acts as a very good trap for electrons.¹ These impurity ions are routinely grown into the alkali halides in order to enhance both the rate of formation and the final concentration of the self-trapped-hole centers when the crystal is irradiated at low temperatures with ionizing radiation x, γ rays, or electrons). The mobile electrons thus produced are quickly trapped by the substitutional Tl^+ impurities forming the paramagnetic $Tl^0(6s^26p^1)$ defects occupying unperturbed positive-ion sites. The rapid trapping inhibits the recombination with the simultaneously produced positive holes which are self-trapped as $\langle 110 \rangle$ oriented $(halogen)_2^-$ centers.²⁻⁴ This unperturbed Tl^0 atom defect on a positive-ion site will be called the "primary $Tl^0(0)$ " defect in this paper.

There is no doubt, e.g., from optical-absorption and luminescence experiments,^{1,5,6} that the primary

$Tl^0(0)$ center exists, but extensive searches have so far failed to yield its electron-spin-resonance (ESR) spectrum, this in spite of the fact that the ESR spectra of the isoelectronic species $Sn^+(5p^1)$,⁷ $In^0(5p^1)$, and $Ga^0(4p^1)$ have been readily observed.^{8,9}

In the course of a systematic investigation of the KCl: Tl^+ system we have found that ionizing radiation produces above 230 K several other types of Tl^0 defects whose ESR spectra are easily observable at low temperatures.^{10,11} Two prominent Tl^0 ESR spectra both of which possess axial symmetry around $\langle 100 \rangle$ are the subject of this experimental and theoretical investigation.

The paper is organized as follows. In Sec. III the analysis of the two Tl^0 ESR spectra is presented. The observed g shifts are quite large but comparable for both centers. The hyperfine (hf) interactions with the thallium nuclei are also large but quantitatively and qualitatively quite different for the two Tl^0 defects. Although the ESR data are by themselves insufficient to determine the defect structures, the

models for the two Tl^0 defects are already presented in Sec. IV in order to facilitate the discussion in the remainder of the paper. Simple arguments are inadequate to explain the difference in hf behavior. Section V presents, therefore, a relativistic many-body calculation of the hf interaction and the g components of the Tl^0 atom both in the free state and in a crystal field of tetragonal symmetry. This is followed in the same section by a discussion of the fitting of the calculations to the experimental g and hf data and by a discussion of the linewidth. Finally, in Sec. VI the x-ray production and thermal data are presented as well as optical F -center excitation experiments. These data together with the analysis of Sec. V fully confirm the models for the Tl^0 defects presented in Sec. IV.

II. EXPERIMENTAL

Several KCl:TlCl crystals were used in this investigation. Some were grown in air by the Kyropoulos method from a melt to which typically about 2 mol% of TlCl was added. An estimate of the actual concentration in the crystal using the height of the Tl^+ absorption band at 247 nm yielded¹ approximately 0.8×10^{-2} mol%. In order to check the possible influence of oxygen impurities on our results two crystals were grown by the Bridgman technique, one in vacuum and the other in a Cl_2 atmosphere in quartz ampoules. Suprapure KCl (Merck) and pure TlCl (UCB) were used as starting materials. A similar estimate of the Tl^+ concentrations yielded 2.2×10^{-2} mol% and 1.5×10^{-2} mol%, respectively. Because the properties of the thallium centers reported in the present paper were similar in all crystals, no further references will be made concerning the growth history of samples. The samples were x irradiated at temperatures between 77 and 320 K using a Siemens

tube with tungsten target (usual settings: 50 kV, 50 mA) and a variable temperature setup described earlier.¹² This setup was also used for pulse-anneal measurements between 200 and 320 K. For pulse anneals to higher temperatures a small temperature stabilized furnace was used. A filter composed of a 1-mm-thin fused-silica plate with a thin aluminum foil wrapped around it was inserted between the sample and the x-ray source in order to absorb the soft x rays.

Before x irradiation the samples were routinely warmed up to about 400 °C for several minutes and then cooled down to room temperature (RT).

The experimental details of the ESR instrumentation have been given elsewhere.¹² It permits measurements at X-band frequencies at temperatures ranging from 10 K to RT.

Optical-absorption measurements were performed on a Cary 14R spectrophotometer equipped with an optical variable temperature cryostat operating between 400 and 77 K.

Selective bleaching of the samples was done at various temperatures in the ESR microwave cavity¹² and also in the optical cryostat. In both cases, monochromatic radiation at various wavelengths was provided by a Bausch and Lomb high intensity monochromator equipped with a 300-nm blaze grating together with corresponding interference or cutoff filters to avoid possible stray light effects. As a light source, use was made of a SP200 high-pressure mercury lamp for the uv region and a 50-W halogen lamp for the visible and ir region. Optical bleaching with linearly polarized light was performed in the 300–900-nm range.

All handling of samples at RT was performed in the dark. During the time the temperature of samples was below 200 K a ambient red illumination of low intensity was employed.

TABLE I. ESR parameters of the $^{205}Tl^0(1)$ and $^{205}Tl^0(2)$ defects in KCl: TlCl at (a) 14 K and (b) 65 K. The hf parameters and the reduced linewidths ΔH are given in mT.

| Defect | g_{\perp} | g_{\parallel} (100) | A_{\perp} | A_{\parallel} (100) | ΔH |
|-----------|----------------------------|--------------------------|--------------------|--------------------------|------------|
| $Tl^0(1)$ | (a) 1.3077 ± 0.0005 | 1.7892 ± 0.0007 | 201.1 ± 0.2 | 372.2 ± 0.4 | 2.7 |
| | (b) 1.293 ± 0.001 | 1.781 ± 0.001 | 208.1 ± 0.3 | 373.3 ± 0.5 | |
| $Tl^0(2)$ | (a) 1.4822 ± 0.0004 | 1.8694 ± 0.0007 | 415.6 ± 0.2 | 113.8 ± 0.1 | 0.75 |
| | (b) 1.4734 ± 0.0004 | 1.8661 ± 0.0004 | 414.3 ± 0.1 | 120.1 ± 0.1 | |

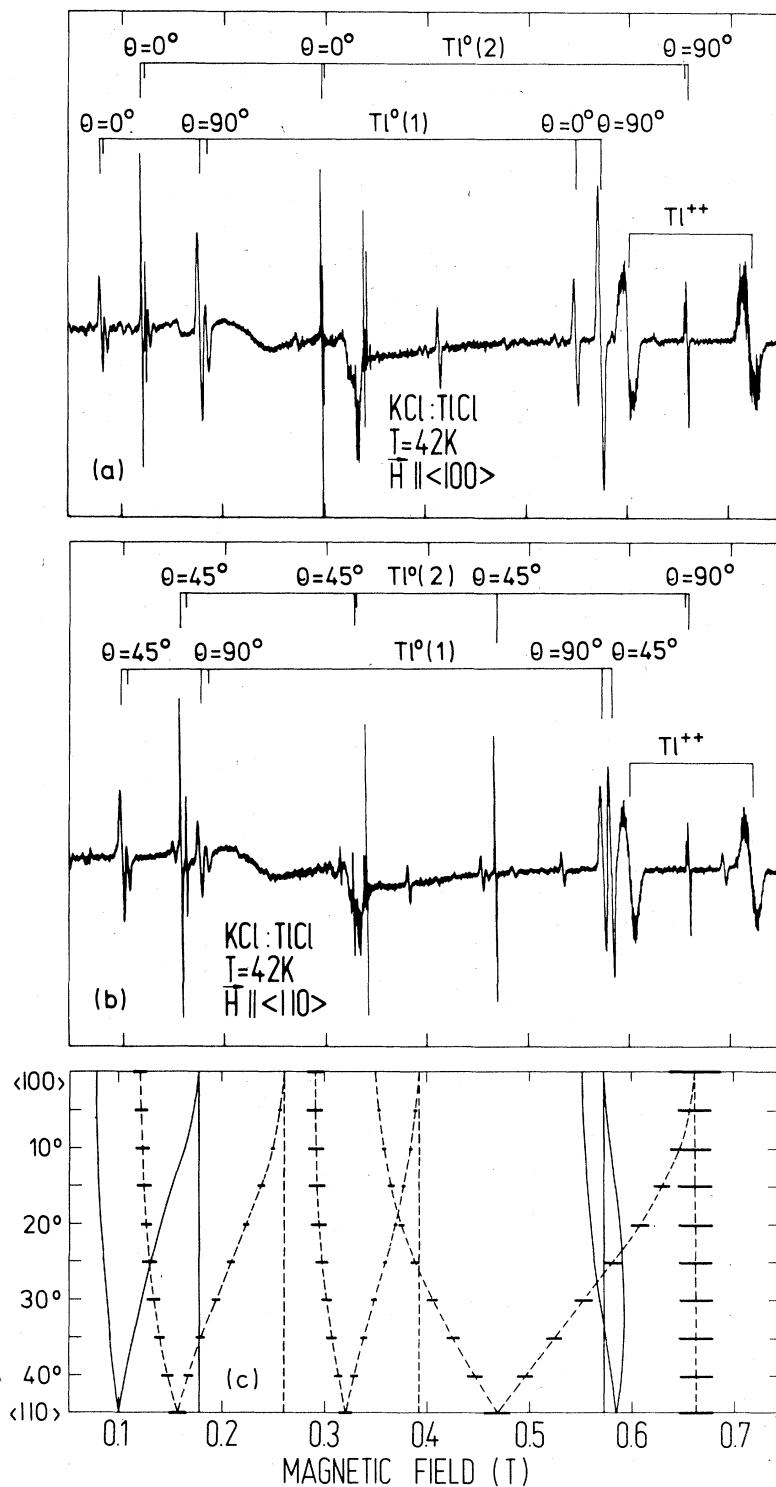


FIG. 1. ESR spectra of $\text{Ti}^{0(1)}$ and $\text{Ti}^{0(2)}$ in KCl:TlCl measured at 42 K after 30 min of x irradiation at RT with (a) $\vec{H} \parallel \langle 100 \rangle$, and (b) $\vec{H} \parallel \langle 110 \rangle$. (c) The calculated angular variation in a $\{100\}$ plane of the ESR spectra of $\text{Ti}^{0(1)}$ and $\text{Ti}^{0(2)}$, indicated by (—) and (---), respectively. The horizontal bars indicate the transition probabilities for $\text{Ti}^{0(2)}$. The intensity variation of the $\text{Ti}^{0(1)}$ lines is small and is not indicated on the figure.

III. ANALYSIS OF THE ESR SPECTRA

A. Production, nomenclature, and description

The properties of two thallium defects, further called $Tl^0(1)$ and $Tl^0(2)$ will be discussed. Their ESR spectra can be observed at ~ 10 K after a short (~ 15 min) x irradiation at RT of Tl^+ -doped KCl crystals. Sometimes, stronger signals can be obtained by a subsequent bleaching in the F band (see Sec. VI). The ESR lines occur between 0.07 and 0.7 T. The width of the lines is the most obvious feature distinguishing the $Tl^0(1)$ and $Tl^0(2)$ spectra, being about 4 and 1 mT, respectively. The experimentally observed linewidths are equal to $(g_0/g)\Delta H$, where ΔH is the true inhomogeneous or reduced width of the ESR line (see Table I).

An angular variation study of the ESR spectra, shows that they both possess axial symmetry around a $\langle 100 \rangle$ crystal direction. Spectra are shown in Figs. 1(a) and 1(b) for the external static magnetic field \vec{H} oriented along $\langle 100 \rangle$ and $\langle 110 \rangle$, respectively. The ESR lines are labeled by the polar angle θ between \vec{H} and the symmetry axis $z \parallel \langle 100 \rangle$ of each defect. In the case of $Tl^0(1)$ one can recognize in Fig. 1 pairs of corresponding high- and low-field transitions originating from a strong hyperfine (hf) coupling between the electron spin and a single nuclear spin $I = \frac{1}{2}$

(both stable thallium isotopes, ^{203}Tl and ^{205}Tl , possess nuclear spin $\frac{1}{2}$). The structure of the $Tl^0(2)$ spectra in Fig. 2 is less transparent than that of the $Tl^0(1)$ spectra. Nevertheless, in both cases a $S = \frac{1}{2}$ spin Hamiltonian, including strong anisotropic hf coupling with a single spin $I = \frac{1}{2}$ nucleus, describes the positions and intensities of the ESR lines (see Sec. III B).

Some of the ESR lines are split in a stronger and a weaker component corresponding to the thallium isotopes ^{205}Tl (70 at. % abundant) and ^{203}Tl (30 at. % abundant), which have nearly equal magnetic moments ($^{205}\mu_I = 1.6274$ and $^{203}\mu_I = 1.6115$ nuclear magnetons¹³). In none of the resonance lines could a superhyperfine (shf) structure be observed, even at the lowest obtainable temperature ($T \approx 8$ K) and at low modulation of the static magnetic field ($\sim 10^{-2}$ mT). All of the line positions are strongly temperature dependent as illustrated by shifts of the order of 10 mT between 10 and 100 K. The linewidths are virtually independent of the temperature and hence it is concluded that if these Tl^0 defects possess an internal motion in this temperature region it is too slow to affect the ESR spectra. Only below $T \approx 15$ K was a weak saturation of the ESR lines observed at full microwave power (~ 200 mW).

B. Spin-Hamiltonian analysis

The ESR spectra of the $Tl^0(1)$ and $Tl^0(2)$ defects are described by the following spin Hamiltonian (usual notation)

$$\frac{\mathcal{H}}{g_0\mu_B} = \frac{1}{g_0} [g_{\perp}(H_x S_x + H_y S_y) + g_{\parallel} H_z S_z] + A_{\perp}(S_x I_x + S_y I_y) + A_{\parallel} S_z I_z, \quad (1)$$

with $S = \frac{1}{2}$ and $I = \frac{1}{2}$. g_{\perp} and g_{\parallel} are principal values of the \vec{g} tensor perpendicular and parallel to the defect symmetry axis $z \parallel \langle 100 \rangle$; A_{\perp} and A_{\parallel} are the corresponding principal values of the hf tensor. For $Tl^0(1)$ the zero-field splittings resulting from the hf interaction are smaller than the microwave energy. Consequently one observes in Fig. 1 high-field and low-field transitions analogous to the "allowed" ESR transitions of a system with weak hf coupling. This is not so for $Tl^0(2)$ for which qualitatively quite different ESR spectra are observed. Only three allowed transitions exist for $\theta = 0^\circ$ or 90° , as is shown in Fig. 1(a). However, at about 0.35 T a transition, forbidden when $\theta = 0^\circ$, becomes progressively allowed when \vec{H} is rotated away from the $\langle 100 \rangle$ direction.

The ESR line positions and intensities were calculated by a numerical computer diagonalization of spin-Hamiltonian Eq. (1) and compared with the experimental position. The g and the hf parameters of $Tl^0(1)$ and $Tl^0(2)$ resulting from a least-squares-

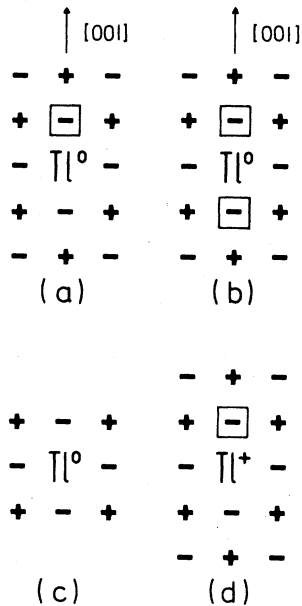


FIG. 2. Schematic representation in a $\{100\}$ plane of (a) the $Tl^0(1)$ and (b) the $Tl^0(2)$ defect, involving one and two anion vacancies, respectively. (c) Model of the primary $Tl^0(0)$ center; (d) proposed model of $Tl^+(1)$, the precursor of $Tl^0(1)$ under electron trapping.

fitting procedure of the line positions measured with $\vec{H} \parallel \langle 100 \rangle$ and $\langle 110 \rangle$, are quoted in Table I for the most abundant isotope ^{205}Tl , and from measurements at 14 and 65 K. The calculated and experimental positions of the ESR lines with $\vec{H} \parallel \langle 100 \rangle$ and $\vec{H} \parallel \langle 110 \rangle$ agree to within 0.2 mT for $\text{Tl}^0(1)$, and to within 0.4 mT for $\text{Tl}^0(2)$. The thallium isotope shifts of the ESR lines were calculated, taking the ^{203}Tl hf parameters to be $^{203}\mu_N/^{205}\mu_N$ times those of ^{205}Tl . The calculated shifts were found to be smaller than the linewidth in all cases where no isotope splitting was observable, and agreed with the measured splitting for the other lines. In Fig. 1(c) a calculated angular variation in a $\{100\}$ plane is shown for both defects including the intensity of the $\text{Tl}^0(2)$ resonance lines, indicated by a horizontal bar. The measured and calculated relative line intensities are sufficiently close to each other, considering the difficulties involved with intensity measurements over such a large magnetic field region.

C. Atomic character of the thallium centers

From the doublet hf structure of the $\text{Tl}^0(1)$ and $\text{Tl}^0(2)$ ESR spectra we concluded already that only one thallium nucleus is present in each of the defects. *A priori* the paramagnetic species most probable to occur are Tl^{2+} , Tl^0 , Tl^- , and maybe Tl^{2-} . For the latter two, a change of the thallium to a negative-ion site must have occurred. Tl^{2+} centers in KCl have been thoroughly studied.^{1,14} They are characterized by a ^2S ground state resulting in isotropic ESR spectra exhibiting strong hf coupling [$A(\text{Tl}^{2+}) = 3.775$ T] and resolved shf interaction with the surrounding halogen ions. None of these properties are observed for the present defects. A Tl^- center with a $6p^2$ ground-state configuration would exhibit an effective spin $S = 0$ or 1 and it would not be possible to fit the ESR spectra to a $S = \frac{1}{2}$ spin Hamiltonian. Finally for $\text{Tl}^{2-}(6p^3)$ one would expect a ^4S ground state, as was found for $\text{Sn}^-(5p^3)$ centers in KCl.¹² In this case a tetragonal crystal-field term must be included in the spin Hamiltonian, and for high strengths of this term one can describe the ESR spectra originating from the ground Kramers doublet by an effective $S = \frac{1}{2}$ formalism. However, the effective g values are then found to be $g_{\parallel} \approx 2$ and $g_{\perp} \approx 4$, or $g_{\parallel} \approx 6$ and $g_{\perp} \approx 0$ depending on the sign of the crystal field. Such g factors are not observed here. So we are led to the $\text{Tl}^0(6p^1)$ hypothesis by exclusion. The g and hf parameters of $\text{Tl}^0(1)$ and $\text{Tl}^0(2)$ are compatible with this identification as will be shown exhaustively in the next section.

Yet a quick qualitative argument supporting the thallium atom identification can already be given. The $\text{Tl}^0(6p^1)$ ground configuration is isoelectronic with $\text{Sn}^+(5p^1)$ whose ESR parameters in KCl have

been determined.⁷ The Sn^+ (tetrag) center in x-irradiated $\text{KCl}:\text{Sn}^{2+}$ exhibits tetragonal symmetry around $\langle 100 \rangle$ and possesses the following g values: $g_{\parallel} = 1.8952$ and $g_{\perp} = 1.6494$. In the Tl^0 center the g values should behave similarly except that the g shifts are expected to be substantially larger because the thallium atom spin-orbit coupling parameter¹⁵ [$\lambda(\text{Tl}^0) \approx 5100 \text{ cm}^{-1}$] is larger than the corresponding Sn^+ parameter⁷ [$\lambda(\text{Sn}^+) \approx 2800 \text{ cm}^{-1}$]. This is indeed observed (see Table I) strongly supporting the $\text{Tl}^0(6p^1)$ atom assignment.

The hf parameters of $\text{Tl}^0(1)$ and $\text{Tl}^0(2)$ are anisotropic and of the same order of magnitude. However, large differences exist in the values of A_{\perp} and A_{\parallel} for the two defects, and especially the inversion of the magnitudes of these two quantities going from $\text{Tl}^0(1)$ to $\text{Tl}^0(2)$ is hard to explain with a simple argument. In Sec. V a relativistic many-body calculation is presented of the hf interaction of a thallium atom in a strong tetragonal electrostatic potential, which represents the crystalline field present in the $\text{Tl}^0(1)$ and $\text{Tl}^0(2)$ centers. It is then possible to account qualitatively and quantitatively for both the g and the hf parameters of the two Tl^0 defects.

IV. MODELS FOR THE $\text{Tl}^0(1)$ AND $\text{Tl}^0(2)$ CENTERS

The discussion at the end of the previous section indicates that the essential constituent of both the $\text{Tl}^0(1)$ and the $\text{Tl}^0(2)$ center is a thallium atom, but the ESR data presented so far do not permit an unambiguous determination of the precise defect structures. Yet one can make a good guess at this point if one takes into account the following observations: (i) the axial symmetry of the ESR spectra around $\langle 100 \rangle$ points to the tetragonal symmetry of the two Tl^0 defects around $\langle 100 \rangle$; (ii) $\text{Tl}^0(1)$ and $\text{Tl}^0(2)$ are not created by x irradiation at, say, 77 K where the primary $\text{Tl}^0(0)$ defect is produced; (iii) the two Tl^0 defects are produced by x irradiation at and above 230 K, room temperature in particular (see Sec. VIB).

Because above 230 K the negative-ion vacancies produced by the x irradiation are very mobile,¹² the last observation strongly points to defect structures for $\text{Tl}^0(1)$ and $\text{Tl}^0(2)$ involving one or more negative-ion vacancies. Figures 2(a) and 2(b) give the precise models that we propose for the $\text{Tl}^0(1)$ and $\text{Tl}^0(2)$ centers. In $\text{Tl}^0(1)$ a Tl^0 atom on a positive-ion site is associated with a single negative-ion vacancy along $\langle 100 \rangle$. In $\text{Tl}^0(2)$ a Tl^0 atom is flanked by two negative-ion vacancies along $\langle 100 \rangle$. In Fig. 2(c) the well-established model for the primary $\text{Tl}^0(0)$ center¹ is also presented. As a mnemonic aid, one notes that in the notation $\text{Tl}^0(0)$, $\text{Tl}^0(1)$, and $\text{Tl}^0(2)$ the number between brackets may be looked upon as giving the number of negative-ion

vacancies involved in the defect.

The models presented in Fig. 2 are strongly supported by the analysis and data presented in the following two sections. We give the models already at this stage in order to facilitate the discussions in the remainder of the paper. Briefly, in Sec. V it is shown that both the qualitative and quantitative features of the hf structure can be understood if the Tl^0 atoms are experiencing crystal fields of the symmetry, sign, and magnitude implied by the models of Figs. 2(a) and 2(b). The thermal, optical, and x-ray production data presented in Sec. VI are also explained in a natural way by the proposed models.

V. CALCULATION OF THE SPIN-HAMILTONIAN PARAMETERS OF THE THALLIUM ATOM CENTERS

The experimental results for the two $Tl^0(6p^1)$ centers in KCl point to a strong influence on the spin-Hamiltonian parameters of the electric field produced by one or more defects (vacancies) in the immediate neighborhood of the thallium atom. Our approach will be to add to the free atom Hamiltonian a strong electrostatic potential term consisting of a first degree and a second degree part with angular dependences $C_0^{(1)}(\theta) = \cos\theta$ and $C_0^{(2)}(\theta) = \frac{1}{2}(3\cos^2\theta - 1)$, respectively (the polar angle θ is taken at the thallium nucleus). These are the only terms that need to be considered in the expansion of a tetragonal crystal field because we will be calculating its effect only between p orbitals, between s and p orbitals, and between s and d orbitals.

Starting with the main interaction mechanisms responsible for the hf interaction of the free atom, the modifications induced by the tetragonal potential are analyzed. The relativistic many-body perturbation procedure presented earlier¹⁶ (and applied to several atomic systems¹⁷⁻¹⁹) is outlined briefly and its application to the Tl^0 centers is extensively discussed.

It is worthwhile to point out that the results concerning the g factors obtained in this section can also be found in a one-electron nonrelativistic treatment. In that case the tetragonal field and the spin-orbit interaction must be diagonalized within the $6p$ states. The usual Zeeman Hamiltonian is then evaluated within the resulting ground doublet.

A. Outline of the many-body approach

Using the restricted relativistic Hartree-Fock (HF) method the one-electron orbitals of the ground configurations ($6s^26p_{1/2}$ and $6s^26p_{3/2}$) of the thallium atom are calculated with Coulthard's method.²⁰ In the next step the so-called V^{N-1} model Hamiltonian,²¹ designated here by H_0 , is constructed in order to generate a set of realistic excited orbitals. This is

done by one-electron excitations from an orbital of the ground configuration which is chosen, if possible, according to the l and j values of the excited orbital to be obtained. Exciting from $6p_{1/2}$ and $6p_{3/2}$ yields the excited $kp_{1/2}$ and $kp_{3/2}$ orbitals ($k > 6$), respectively. In the same way the kd and kf functions are obtained from $5d$ and $4f$ excitations with corresponding j values. The $kg_{7/2}$ orbital was calculated from a $6p_{1/2}$ excitation. Bound-state solutions up to $k = 12$ were calculated as well as fifteen continuum solutions belonging to appropriate wave numbers.

The $6p_{1/2}$ and $6p_{3/2}$ states of the ground configuration ($6p^1$) are now improved by a perturbation treatment using the set of all many-electron states that can be constructed from the ground and excited orbitals described above. The difference $\Delta\mathcal{H} = \mathcal{H} - \mathcal{H}_0$ between the actual free atom Hamiltonian, \mathcal{H} , and the model Hamiltonian, \mathcal{H}_0 , is the perturbation Hamiltonian. The effect of the inclusion of one-electron excitations only is very similar to the unrestricted relativistic HF results. Pair excitations are also considered; they describe the correlation effects.

The one-electron Dirac orbitals are chosen to have the form:

$$\Phi_{lsm} = \begin{pmatrix} \frac{P_j(r)}{r} \chi_{jm^+}(\theta, \phi) \\ i \frac{Q_j(r)}{r} \chi_{jm^-}(\theta, \phi) \end{pmatrix} \quad (2)$$

$P_j(r)$ and $Q_j(r)$ are the large- and small-component radial functions. $\chi_{jm\pm}$ represent the ls -coupled eigenfunctions of \vec{j}^2 and j_z , where the (+) signs stand for $(l,s)j$ coupling, and the (-) signs stand for either $(l+1,s)j$ or $(l-1,s)j$ coupling depending on whether $j = l + \frac{1}{2}$ or $l - \frac{1}{2}$, respectively.

B. Magnetic hf interaction of the free Tl^0

The magnetic hf interaction Hamiltonian, describing both the dipole-dipole and the contact contributions is given by

$$\mathcal{H}_{\text{hf}} = \sum_{i=1}^{81} h_{\text{hf}}(i) \quad (3a)$$

in which each one-electron Hamiltonian has the form

$$h_{\text{hf}} = \frac{1}{2c} \frac{\vec{\alpha} \cdot (\vec{\mu}_I \times \vec{r})}{r^3} \quad (3b)$$

where for simplicity the summation symbol on $\vec{\alpha}$ (the four-dimensional Dirac velocity operator) and \vec{r} (the position vector of each electron) has been deleted. Energies are calculated in Hartree units (27.2 eV) where $c = 137.036$ is the inverse of the fine structure constant. $\vec{\mu}_I = \mu_I(\vec{I}/I)$ is the magnetic moment of the thallium nucleus, both isotopes of

which possesses a nuclear spin $I = \frac{1}{2}$, and $^{205}\mu_I = 8.863 \times 10^{-4}$ Bohr magnetons (μ_B) and $^{203}\mu_I = 8.776 \times 10^{-4}\mu_B$. In the present units $\mu_B = 1/2c$.

By writing out in detail the expressions (3a) and (3b) it is straightforward to derive explicit formulas for the matrix elements $\langle jm | h_{\text{hf}} | j'm' \rangle$ of h_{hf} between the Dirac orbitals. In Ref. 16 the diagonal elements are given. Therefore only the following nondiagonal ones are presented here (the components of $\bar{\mathbf{I}}$ are still to be evaluated):

$$\langle j m + 1 | h_{\text{hf}} | j' m \rangle = -iR_{jj'} A_{jj'}^{m+1 m}, \quad (4)$$

with

$$R_{jj'} = \int r^{-2} [P_j(r) Q_{j'}(r) + P_{j'}(r) Q_j(r)] dr, \quad (5)$$

$$A_{jj'}^{m+1 m} = \frac{2il[l^2 - (m + \frac{1}{2})^2]^{1/2}}{4l^2 - 1} \frac{I_x - iI_y}{I} \frac{\mu_I}{2c} \quad (6)$$

for

$$j = l - 1/2, \quad j' = j, \quad l' = l,$$

$$A_{jj'}^{m+1 m} = \frac{-2i(l+1)[(l+1)^2 - (m + \frac{1}{2})^2]^{1/2}}{(2l+1)(2l+3)} \times \frac{I_x - iI_y}{I} \frac{\mu_I}{2c} \quad (7)$$

for

$$j = l + 1/2, \quad j' = j, \quad l' = l,$$

$$A_{jj'}^{m+1 m} = \frac{i[(l-m)^2 - \frac{1}{4}]^{1/2}}{4l+2} \frac{I_x - iI_y}{I} \frac{\mu_I}{2c} \quad (8)$$

for

$$j = l - 1/2, \quad j' = l + 1/2, \quad l' = l,$$

and ultimately

$$A_{jj'}^{m+1 m} = \frac{-i[(l+1+m)^2 - \frac{1}{4}]^{1/2}}{4l+2} \frac{I_x - iI_y}{I} \frac{\mu_I}{2c} \quad (9)$$

for

$$j = l + 1/2, \quad j' = l - 1/2, \quad l' = l.$$

The radial elements $R_{jj'}$ between the $6p_{1/2}$ and $6p_{3/2}$ orbitals are calculated from the HF solution of the ground configuration of Ti^0 and the resulting hf coupling parameters are presented in Table II. They are compared to results of atomic beam experiments on the free $^{203}\text{Ti}^0$ atom.^{22, 23}

The impressive disagreement of the HF value compared to the experimental value for the $j = \frac{3}{2}$ state²² has been known for a long time: it was discussed in the literature as early as 1933.²⁴ It seems that a

TABLE II. Radial matrix elements $R_{jj'}$, of the relativistic HF $6p$ orbitals of the free Ti^0 atom; calculated lowest-order hf coupling parameters, A_{calc} , compared to the experimental hf results, A_{expt} (from Refs. 22 and 23) both for the ^{203}Ti isotope.

| j | j' | $R_{jj'}$ | A_{calc} (MHz) | A_{expt} (MHz) |
|---------------|---------------|-----------|----------------------------|----------------------------|
| $\frac{1}{2}$ | $\frac{1}{2}$ | 0.3432 | 19 272 | 21 130 |
| $\frac{3}{2}$ | $\frac{1}{2}$ | 0.0379 | ... | |
| $\frac{3}{2}$ | $\frac{3}{2}$ | -0.061 41 | 1 377 | 262 |

first-principles calculation was not attempted until very recently by Ray *et al.*²⁵ and by Sushkov *et al.*²⁶ In the former work it was found that there are two highly competing mechanisms that correct the pure HF results. The first consists of polarization of the occupied s shells by the unpaired $6p$ electrons described in this formalism by single excitations of an electron from an occupied s orbital to an excited one: $ns \rightarrow ks$ ($n \leq 6$; $k > 6$). This exchange-core-polarization (ECP) effect contributes -3061 MHz to the $6p_{3/2}$ hf coupling.²⁵ The second mechanism originates from the correlation between the electrons which is partly described by pair excitations from the ground configuration. From a calculation of the lowest-order correlation terms, and of some of the higher-order ones which are considered to be most important,²⁵ a contribution of $+2000$ MHz was found. In particular the pair excitations described schematically by $6s6p_j^m \rightarrow k d 6p_j^{m'}$ proved to be crucial, but also $6s6p_j^m \rightarrow ks6p_j^{m'}$ and $5d6s \rightarrow 6p k f$ contributed substantially. The total calculated $p_{3/2}$ hf coupling is $+320$ MHz. The error on the correlation contribution is estimated to be smaller than 15%. This yields an uncertainty on the calculated hf interaction comparable to the experimental value. It is, however, felt that the very low $6p_{3/2}$ hf coupling is theoretically understood and that the difference between the HF and experimental values is entirely due to the two effects described above.

The contributions to the $6p_{1/2}$ hf coupling are quite different from those of the $6p_{3/2}$ state. The correlation term is nearly unchanged, but the ECP effect is smaller and both cancel to almost zero. This is in agreement with the experimental value of the hf anomaly between the $6p_{1/2}$ and $6p_{3/2}$ states.²² The difference of 1858 MHz between HF and experimental hf coupling is now found to be almost entirely due to polarization of the $4p_{1/2}$ and $5p_{1/2}$ shells. Similar effects were found by Desclaux and Bessis for the

$4p_{1/2}$ state of $\text{Ga}^{0.27}$

The ECP and correlation effects mix Slater determinants corresponding to one- and two-electron excitations in the HF ground state. However, it turns out that the final improved states of the ground configuration are still pure $6s^26p_j$ to about 96%.

C. Inclusion of the crystal field

It will now be assumed that the ground state of Ti^0 is modified by an electrostatic field generated by a pair of charges e_1 and e_2 located on the z axis at a distance R_0 at both sides of the atom. We will retain only the first- and second-degree terms in the expansion of the field acting on each electron in the neighborhood of the atom

$$v_c(\bar{r}) = q_1 a(r) C_0^{(1)}(\theta) + q_2 b(r) C_0^{(2)}(\theta), \quad (10)$$

with

$$a(r) = \frac{r_{<}}{r_{>}^2}, \quad b(r) = \frac{r_{<}^2}{r_{>}^3} \quad (11)$$

and

$$q_1 = e_1 - e_2, \quad q_2 = e_1 + e_2. \quad (12)$$

$$C_0^{(1)}(\theta) = \cos\theta$$

and

$$C_0^{(2)}(\theta) = \frac{1}{2}(3\cos^2\theta - 1),$$

following the definition of the angular functions $C_m^{(2)}$ given by Edmonds.²⁸ $r_{<}$ and $r_{>}$ are the smaller and the larger one, respectively, of the distance r of the electron from the nucleus, and of the distance R_0 .

The crystal-field v_c causes a strong mixing of the $6p_{1/2}$ and $6p_{3/2}$ orbitals, which is not well described by a perturbation treatment. Therefore we first diagonalize the one-electron Hamiltonian

$$h = h_0 - e v_c \quad (13)$$

between the six $6p$ one-electron functions. h_0 is the HF Hamiltonian appropriate for the $6p$ orbital and we take the electron charge $e = 1$ in the calculations to follow. Due to the axial symmetry of v_c , matrix elements $\langle jm | v_c | j'm' \rangle$ are zero unless $m = m'$. Therefore only two identical 2×2 matrices must be diagonalized, e.g., for $m = \frac{1}{2}$:

| j | $\frac{1}{2}$ | $\frac{3}{2}$ |
|---------------|------------------------------|--------------------------------------|
| $\frac{1}{2}$ | $\epsilon_{1/2}$ | $-\frac{1}{5}\sqrt{2}q_2b_1$ |
| $\frac{3}{2}$ | $-\frac{1}{5}\sqrt{2}q_2b_1$ | $\epsilon_{3/2} + \frac{1}{5}q_2b_2$ |

(14)

$\epsilon_{1/2}$ and $\epsilon_{3/2}$ are the one-electron HF energies of $6p_{1/2}$ and $6p_{3/2}$. b_1 and b_2 are defined by

$$b_1 = -\langle P_{1/2}, Q_{1/2} || b(r) || P_{3/2}, Q_{3/2} \rangle, \quad (15a)$$

$$b_2 = -\langle P_{3/2}, Q_{3/2} || b(r) || P_{3/2}, Q_{3/2} \rangle, \quad (15b)$$

using the notation

$$\langle f_1, f_2 || F(r) || g_1, g_2 \rangle = \int (f_1 g_1 + f_2 g_2) F(r) dr.$$

The b_1 and b_2 parameters are comparable to each other; in the nonrelativistic approximation they are equal. From Eq. (14) and from the analogous $m = -\frac{1}{2}$ matrix, the new ground-state orbitals of the $6p$ electron form the Kramers doublet

$$\phi_{p+} = K_1 p_{1/2}^{1/2} + K_2 p_{3/2}^{1/2}, \quad (16a)$$

$$\phi_{p-} = K_1 p_{1/2}^{-1/2} - K_2 p_{3/2}^{-1/2}, \quad (16b)$$

with

$$\frac{K_1}{K_2} = \frac{\frac{1}{5}\sqrt{2}q_2b_1}{\epsilon_{1/2} - \epsilon}, \quad (17)$$

and in which ϵ is the lowest eigenvalue of matrix (14). For a Ti^0 atom in the field v_c the g values are essentially determined by this mixing of $6p_{1/2}$ and $6p_{3/2}$. However, this mixing is also influenced by the first-degree field associated with the charge q_1 , through a second-order effect involving excited s and d states. This can be described by an effective second-degree field associated with an effective charge αq_1^2 . The effect of some of the nearest excited s and d states was calculated and this yields the approximate value $\alpha = 0.5 \pm 0.1$. The mixing of the $6p$ orbitals by the second-order effect of the first-degree field will be absorbed in the constants b_1 and b_2 (Eqs. (15) and consequently in the coefficients K_1 and K_2 (Eq. (17) by replacing in matrix (14) q_2 by

$$q_2^{\text{eff}} = q_2 + \alpha q_1^2. \quad (18)$$

In addition to the mixing of the $6p$ orbitals there is a smaller mixing of excited configurations like $6s6pkd$ or $6s^2ks$ in the ground configuration. This has a small effect on the g parameters, but it contributes substantially to the hf coupling parameters. The new ground state, using the $\phi_{p\pm}$ orbitals is improved by a perturbation treatment using as perturbing Hamiltonian

$$\Delta\mathcal{H}' = \mathcal{H} - \mathcal{H}_0 - e \sum_{i \neq 6p} v_c(\bar{r}_i)$$

in a way analogous to the treatment of the free atom. The part of the crystal-field operator applying to the $6p$ orbital was taken into account by the diagonalization of matrix (14).

D. Calculation of the g parameters of the spin Hamiltonian

We sketch the procedure for $g_{\parallel} \equiv g_z$; for g_{\perp} the calculation is similar. The relativistic Hamiltonian describing the magnetic interaction of an electron at $\vec{r}(x,y,z)$ with an external magnetic field $\vec{H} = H_z \vec{e}_z$ is given by

$$h_z = \frac{1}{2}(\alpha_y x - \alpha_x y) H_z, \quad (19a)$$

or equivalently

$$h_z = \frac{-i}{2\sqrt{2}} [\alpha_+ r C_1^{(-1)}(\theta, \phi) + \alpha_- r C_1^{(1)}(\theta, \phi)] H_z. \quad (19b)$$

It is straightforward to calculate g_{\parallel} by a comparison of matrix elements of Eq. (19b) in the basis Eq. (16) with those of $g_{\parallel} \mu_B S_z H_z$ in the basis of spin functions used in the spin Hamiltonian. The following expressions are found:

$$g_{\parallel}^{(0)} = \frac{2}{3} K_1^2 + \frac{4}{3} K_2^2 - \frac{4}{3} \sqrt{2} K_1 K_2 \Sigma, \quad (20a)$$

$$g_{\perp}^{(0)} = \left| \frac{2}{3} K_1^2 - \frac{8}{3} K_2^2 + \frac{2}{3} \sqrt{2} K_1 K_2 \Sigma \right|, \quad (20b)$$

in which Σ is defined by

$$\Sigma = -c \langle P_{1/2}, Q_{1/2} || r || Q_{3/2}, P_{3/2} \rangle. \quad (21)$$

Σ is almost equal to unity ($\Sigma = 0.98$) for Ti^0 . Note

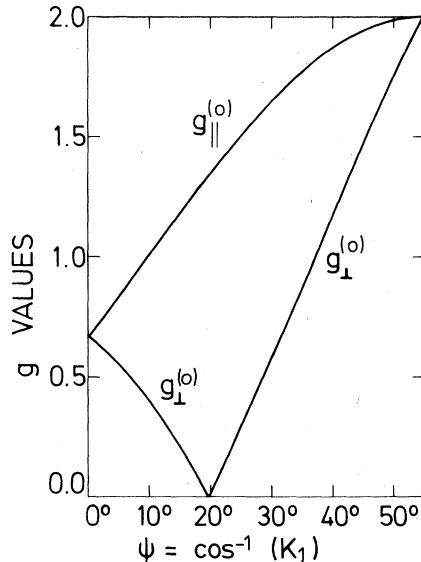


FIG. 3. g values $g_{\perp}^{(0)}$ and $g_{\parallel}^{(0)}$, resulting from the mixing of the $6p$ orbitals of the Ti^0 atom by the crystal field v_c , are given as a function of the angle $\psi = \cos^{-1}(K_1)$. The mixing coefficient K_1 is given in Eq. (17) as a function of the crystal-field matrix elements $b_1 q_2$ and $b_2 q_2$, and of the free-atom energy splitting $\epsilon_{1/2} - \epsilon_{3/2}$.

that through q_2^{eff} as given in Eq. (18), g_{\parallel} and g_{\perp} depend on q_1 .

Two limiting cases are easily checked using Eqs. (17) and (20). The ground state of the free atom is a $6p_{1/2}$ state ($K_1 = 1, K_2 = 0$) and in agreement with Landé's formula one finds $g_{\perp} = g_{\parallel} = \frac{2}{3}$. For a large and positive value of q_2 the orbital angular momentum is quenched because the spin-orbit energy is small compared to the crystal-field energy; consequently, in a nonrelativistic approximation ($b_1 = b_2$ and $\Sigma = 1$) one finds $K_1 = +\sqrt{1/3}$ and $K_2 = -\sqrt{2/3}$ and so $g_{\parallel} \approx g_{\perp} \approx 2$. In Fig. 3 g_{\perp} and g_{\parallel} are displayed as a function of $\psi = \cos^{-1}(K_1)$ for values between these two limits. These results can be compared with the calculation of Ammeter and Schlosnagle,²⁹ concerning the g values of axial Ga^0 defects in rare-gas matrices.

E. Calculation of the A parameters of the spin Hamiltonian

The analysis of the contributions to the hf coupling in the framework of perturbation theory is conveniently performed using Feynman diagrams. The analysis is given in Figs. 4 and 5. In Fig. 4 the contributions are given that are also present in the free atom but evaluated using the crystal-field mixed $\phi_{p\pm}$ states (which in the diagrams are drawn as a double arrow) whereas the additional ones are given in Fig. 5. Because we are primarily interested in the physical effects and for practical reasons not so much in accu-

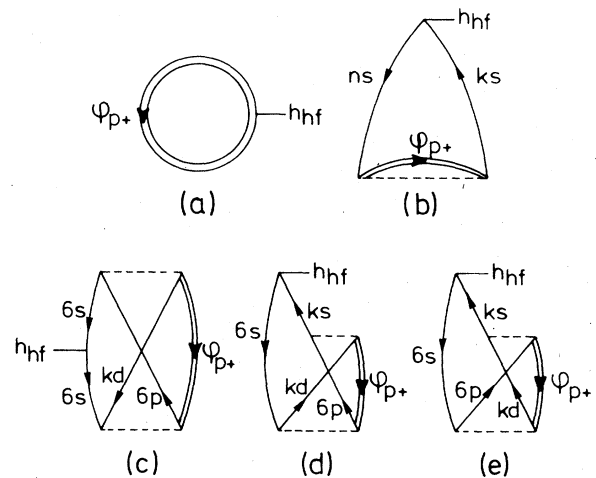


FIG. 4. Feynman diagrams representing the contributions to the hf interaction of the Ti^0 atom, which do not involve the crystal-field v_c explicitly. Note that the $6p$ orbital, which would occur in the free-atom diagrams, is replaced by the "solid-state" orbital ϕ_{p+} .

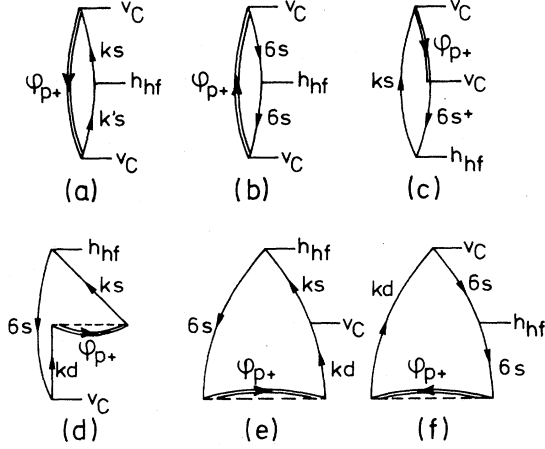


FIG. 5. Major contributions to the hf interaction of the Ti^0 atom, involving the first-degree [diagrams (a), (b), and (c)] and the second-degree [(d), (e), and (f)] part of the crystal-field v_c .

racy, only the lowest-order contributions are given. In this subsection we always take $n \leq 6$ and $k > 6$. The leading contribution is given in Fig. 4(a) and we call it the direct contribution of the crystal-field mixed $\phi_{p\pm}$ to the hf coupling. The hf formulas can be derived using Eqs. (4)–(9) and (16). The result

$$A_{\parallel}^{(2)} = -\frac{4}{I} \sum_{nkm_s} \frac{\langle ns, I | h_{hf} | ks, I \rangle \langle ks; \phi_{p+} | 1/r_{12} | \phi_{p+}; ns \rangle}{\epsilon_{ns} - \epsilon_{ks}}, \quad (23a)$$

$$A_{\perp}^{(2)} = -\frac{4}{\sqrt{2}I} \sum_{nk} \frac{\langle ns^+, I-1 | h_{hf} | ks^-, I \rangle \langle ks^-; \phi_{p+} | 1/r_{12} | \phi_{p-}; ns^+ \rangle}{\epsilon_{ns} - \epsilon_{ks}}. \quad (23b)$$

In the two-electron elements the first function of the bra and ket belongs to electron 1, the second to electron 2; m_s indicates the spin states of the ks and ns orbitals, which must be equal.

Combining Eqs. (4) to (9) for h_{hf} with Eq. (16) for $\phi_{p\pm}$ the following expressions are obtained:

$$A_{\parallel}^{(2)} = -\frac{\mu_I}{I} \frac{1}{2c} \left(\frac{8}{27} K_1^2 F_{1/21/2} - \frac{8}{27} K_2^2 F_{3/23/2} + \frac{32}{27} \sqrt{2} K_1 K_2 F_{3/21/2} \right), \quad (24a)$$

$$A_{\perp}^{(2)} = -\frac{\mu_I}{I} \frac{1}{2c} \left(\frac{8}{27} K_1^2 F_{1/21/2} + \frac{16}{27} K_2^2 F_{3/23/2} - \frac{16}{27} \sqrt{2} K_1 K_2 F_{3/21/2} \right), \quad (24b)$$

with

$$F_{jj'} = \sum_{nk} \frac{R_{nk} \left\langle P_k, Q_k; P_j, Q_j \left\| \frac{r_{<}}{r_{>}^2} \right\| P_j, Q_j; P_n, Q_n \right\rangle}{\epsilon_{ns} - \epsilon_{ks}}. \quad (24c)$$

If Eqs. (24) are asymmetric in j and j' , $F_{jj'}$ is replaced by $\frac{1}{2}(F_{jj'} + F_{j'j})$. R_{nk} is similar to the $R_{jj'}$ defined earlier in Eq. (4). $r_{<}$ and $r_{>}$ are the smaller and the larger of the radii r_1 and r_2 . Through the use of a semicolon the radial element of $1/r_{12}$ is written in such a way that the two-electron nature is shown. Here and in the following we write

$$\langle f_1, f_2; f_3, f_4 || W(1, 2) || g_1, g_2; g_3, g_4 \rangle = \int \int dr_1 dr_2 W(1, 2) [f_1(1)g_1(1) + f_2(1)g_2(1)] [f_3(2)g_3(2) + f_4(2)g_4(2)] \quad (25)$$

is

$$A_{\parallel}^{(1)} = \frac{\mu_I}{I} \frac{1}{2c} \left(\frac{4}{3} K_1^2 R_{1/21/2} - \frac{8}{15} K_2^2 R_{3/23/2} + \frac{4}{3} \sqrt{2} K_1 K_2 R_{3/21/2} \right), \quad (22a)$$

$$A_{\perp}^{(1)} = \frac{\mu_I}{I} \frac{1}{2c} \left(\frac{4}{3} K_1^2 R_{1/21/2} + \frac{16}{15} K_2^2 R_{3/23/2} - \frac{2}{3} \sqrt{2} K_1 K_2 R_{3/21/2} \right). \quad (22b)$$

To compare with nonrelativistic formulas valid to a large extent for atoms with $(Z/c)^2 \ll 1$, one can use the correspondences

$$R_{1/21/2} \simeq 4 \langle r^{-3} \rangle_{\mu_B}, \quad R_{3/23/2} \simeq -2 \langle r^{-3} \rangle_{\mu_B},$$

$$R_{3/21/2} \simeq \langle r^{-3} \rangle_{\mu_B},$$

in which the averages are performed over the nonrelativistic $6p$ orbital. The diagram 4(b) represents the very important ECP effect. Especially the $6s$ orbital is found to contribute substantially. Represented by diagrams 4(c) to 4(e) are the major correlation contributions as mentioned in Sec. VB. They are opposite in sign to the ECP terms represented by diagram 4(b). However, many more smaller contributions have been taken into account.

It can be shown that these four diagrams have a similar dependence on K_1, K_2 : Only the radial matrix elements are different. Therefore only the formulas for the diagram 4(b) are explicitly derived.

From this diagram one can read the following contributions to A_{\parallel} and A_{\perp} :

The diagrams 4(c) to 4(e) only differ among each other in the radial functions $F_{jj'}$. The diagrams 5(a) and 5(f) represent additional contributions that result from polarization of the atom by the crystal field; Figs. 5(a) to 5(c) give the influence of the first-degree field in the lowest order. There are two other members where the h_{hf} vortex has to be drawn in the $\phi_{p\pm}$ line in Figs. 5(a) and 5(b) but these are con-

tained in the effective second-degree field mentioned earlier. There are higher order contributions of the first-degree field that one can obtain by introducing first-degree field vertices in Figs. 4(b) to 4(e). These were found to be sufficiently small to be negligible.

As an example of the contributions involving the first-degree field, diagram 5(a) is written out explicitly (adding the other diagrams will only change the radial elements):

$$A_{\parallel}^{(3)} = \frac{2}{I} \sum_{k'km_s} \frac{\langle ks, I | h_{hf} | k's, I \rangle \langle \phi_{p+} | v_c | ks \rangle \langle k's | v_c | \phi_{p+} \rangle}{(\epsilon - \epsilon_{ks})(\epsilon - \epsilon_{k's})} \quad (26a)$$

$$A_{\perp}^{(3)} = \frac{2}{\sqrt{2}I} \sum_{k'k} \frac{\langle ks^+, I-1 | h_{hf} | k's^-, I \rangle \langle \phi_{p+} | v_c | ks^+ \rangle \langle k's^- | v_c | \phi_{p-} \rangle}{(\epsilon - \epsilon_{ks})(\epsilon - \epsilon_{k's})} \quad (26b)$$

Again m_s indicates the spin state of the ks and $k's$ orbitals. This yields the following explicit expressions:

$$A_{\parallel}^{(3)} = q_2^2 \frac{\mu_I}{I} \frac{1}{2C} \left(-\frac{4}{27} K_1^2 G_{1/2,1/2} - \frac{8}{27} K_2^2 G_{3/2,3/2} + \frac{8}{27} \sqrt{2} K_1 K_2 G_{1/2,3/2} \right) \quad (27a)$$

$$A_{\perp}^{(3)} = -A_{\parallel}^{(3)} \quad (27b)$$

and

$$G_{jj'} = \sum_{kk'} \frac{R_{kk'} \langle P_j, Q_j | a(r) | P_k, Q_k \rangle \langle P_k, Q_k | a(r) | P_{j'}, Q_{j'} \rangle}{(\epsilon - \epsilon_{ks})(\epsilon - \epsilon_{k's})} \quad (27c)$$

in which ϵ is the energy of the $\phi_{p\pm}$ orbitals. Finally, we have the important modification of the ECP contribution to the hf parameters by the second-degree field given in Figs. 5(a) to 5(f). It was found that similar modifications based on the correlation diagrams 4(c) to 4(e) are not very important; so we neglect them.

The following expressions are deduced from Fig. 5(d):

$$A_{\parallel}^{(4)} = q_2 \frac{\mu_I}{I} \frac{1}{2C} \left(\frac{32}{135} K_1^2 H_{1/2,1/2} + \frac{8}{27} K_2^2 H_{3/2,3/2} - \frac{16}{135} \sqrt{2} K_1 K_2 H_{3/2,1/2} \right) \quad (28a)$$

$$A_{\perp}^{(4)} = q_2 \frac{\mu_I}{I} \frac{1}{2C} \left(-\frac{16}{135} K_1^2 H_{1/2,1/2} - \frac{32}{135} K_2^2 H_{3/2,3/2} + \frac{32}{135} \sqrt{2} K_1 K_2 H_{3/2,1/2} \right) \quad (28b)$$

with

$$H_{jj'} = - \sum_{6skd} \frac{R_{ks6s} \langle P_{6s}, Q_{6s} | b(r) | P_{kd}, Q_{kd} \rangle \left\langle P_{kd}, Q_{kd}; P_j, Q_j \left\| \frac{r_{<}}{r_{>}} \right\| P_{j'}, Q_{j'}; P_{ks}, Q_{ks} \right\rangle}{(\epsilon_{6s} - \epsilon_{kd})(\epsilon_{kd} - \epsilon_{ks})} \quad (28c)$$

$H_{jj'}$ is again replaced by $(H_{jj'} + H_{j'j})/2$ if Eq. (32) is not symmetric in j and j' . Since the large component radial functions of the $kd_{3/2}$ and $kd_{5/2}$ orbitals are nearly equal, the corresponding radial elements were taken to be the same.

The diagrams 5(e) and 5(f) yield formally the same expressions as 5(d) but with different radial integrals.

F. Analysis of the experimental g and hf parameters

In order to explain the striking difference between the experimentally observed hf parameters of the

Ti⁰(1) and the Ti⁰(2) centers (Table I) we will use the model that we constructed in the foregoing subsections involving the influence of the crystal field on the ground-state magnetic properties of Ti⁰. The two charges e_1 and e_2 along the z axis, which produce the crystal field [Eqs. (10), (11), and (12)], represent then the effective charges of the negative-ion vacancies involved in the models of the centers (see Fig. 2). In a purely ionic model, without polarization of the lattice, one would expect a unit positive charge for such a vacancy at the NN distance of KCl from the Ti⁰ atom: $R_0 = 5.95$ a.u. Thus $e_1 = 1$ and $e_2 = 0$ (which means $q_1 = q_2 = 1$) would apply to the Ti⁰(1)

center and $e_1 = e_2 = 1$ (which means $q_1 = 0$ and $q_2 = 2$) to $Tl^0(2)$. Because, as we will demonstrate below, the thallium valence electron is partly delocalized in an F -center-like orbital on the negative-ion vacancies, the charge of the latter is not well described by a unit point charge; furthermore there can be polarization effects. Thus, significant departures from these ideal e_1 and e_2 values are possible and even likely. The delocalization should be approached from a molecular orbital point of view involving a sufficiently large cluster of appropriately displaced K^+ and Cl^- ions surrounding the thallium atom. This falls outside the scope of the present approach. Within our atomic approach we will describe the delocalization in a rather *ad hoc* manner by introducing a localization factor f : the delocalized part $1 - f$ of the Tl^0 valence electron contributes to the g factor with nearly the free-electron value $g_0 = 2$ (the

spin-orbit parameters for K^+ and Cl^- are indeed small compared to that of Tl^0); the localized part, f , on the Tl^0 contributes to the g and hf parameters with an amount given by Eqs. (20), (22), (24), (27), and (28). We obtain

$$g_{\perp} = fg_{\perp}^{(0)} + (1 - f) , \quad (29)$$

$$A_{\perp} = fA_{\perp}^{(0)} = f(A_{\perp}^{(1)} + A_{\perp}^{(2)} + A_{\perp}^{(3)} + A_{\perp}^{(4)}) , \quad (30)$$

and completely analogous relations for g_{\parallel} and A_{\parallel} .

The radial matrix elements needed for the calculation of the hf components are listed in Table III. The summation over all diagrams of a given family is already performed. After conversion to the notation and units ($\{^{205}\mu_I/I\}[1/(2c)] = 1521 \text{ T/a.u.}$) of the spin-Hamiltonian Eq. (1) we find, for the ^{205}Tl isotope, in mT units:

$$A_{\parallel}^{(0)} = 762K_1^2 + 10K_2^2 + 223K_1K_2 + q_1^2(140K_1^2 + 310K_2^2 - 417K_1K_2) + q_2(-59K_1^2 - 75K_2^2 + 42K_1K_2) , \quad (31a)$$

$$A_{\perp}^{(0)} = 762K_1^2 - 19K_2^2 - 112K_1K_2 - q_1^2(140K_1^2 + 310K_2^2 - 417K_1K_2) + q_2(30K_1^2 + 60K_2^2 - 84K_1K_2) . \quad (31b)$$

In order to calculate $K_1(\alpha; q_1, q_2)$ and $K_2(\alpha; q_1, q_2)$ one needs the following eigenvalues and matrix elements (between the $6p$ HF functions):

$$\epsilon_{1/2} = -0.2134, \quad \epsilon_{3/2} = -0.1777 , \quad (32)$$

$$b_1 = -0.0714, \quad b_2 = -0.0649 , \quad (33)$$

in units of a.u.

It is a consequence of our *ad hoc* description of delocalization that the ratio $\gamma(\alpha; q_1, q_2) = A_{\perp}/A_{\parallel}$ is independent of the localization factor f . We will exploit this by investigating the behavior of this ratio as a function of q_1 and q_2 . In Fig. 6 a set of lines of constant γ is drawn in the (q_1, q_2) plane using the estimated value $\alpha = 0.5$. This set includes the lines corresponding to the experimental hf parameters of $Tl^0(1)$, $\gamma = 0.540$, and of $Tl^0(2)$, $\gamma = 3.653$. These

lines are quite insensitive to the value of α , i.e., to the effective second-degree field induced by the first-degree field. This is illustrated in Fig. 6: the lines corresponding to $\alpha = 0.75$ and 0.25 do not differ much from the $\alpha = 0.5$ line especially for the larger q_2 values. For the $\gamma = 3.653$ curve these deviations are even smaller because of the smallness of the associated q_1 value.

From Fig. 6 it can be concluded that the hf ratio $\gamma = 0.540$ corresponding to $Tl^0(1)$ can only be obtained for q_1 values in the narrow range $+0.8$ to $+1.0$ but virtually any q_2 value ranging from 0 to 2 is possible. Its value must be obtained from a fit of the g factors. In contrast to this, the $\gamma = 3.653$ curve appropriate for $Tl^0(2)$ is only defined for $q_2 \geq +1.84$ and rather small q_1 values ($q_1 < +0.45$ for $q_2 \leq +2.4$).

TABLE III. List of radial matrix elements (in a.u.) contributing to the hf interaction in the Tl^0 atom in an axial crystal field. Distance of the charges is 5.95 a.u.

| j | j' | $R_{jj'}$ | $F_{jj'}$ | $G_{jj'}$ | $H_{jj'}$ |
|---------------|---------------|--------------------|-----------|-----------|-----------|
| $\frac{1}{2}$ | $\frac{1}{2}$ | 0.376 ^a | ~ 0 | -0.624 | -0.164 |
| $\frac{3}{2}$ | $\frac{1}{2}$ | 0.0379 | -0.0450 | -0.656 | -0.165 |
| $\frac{3}{2}$ | $\frac{3}{2}$ | -0.0619 | -0.0902 | -0.690 | -0.166 |

^a $3p_{1/2}4p_{1/2}$ and $5p_{1/2}$ ECP contributions are included here.

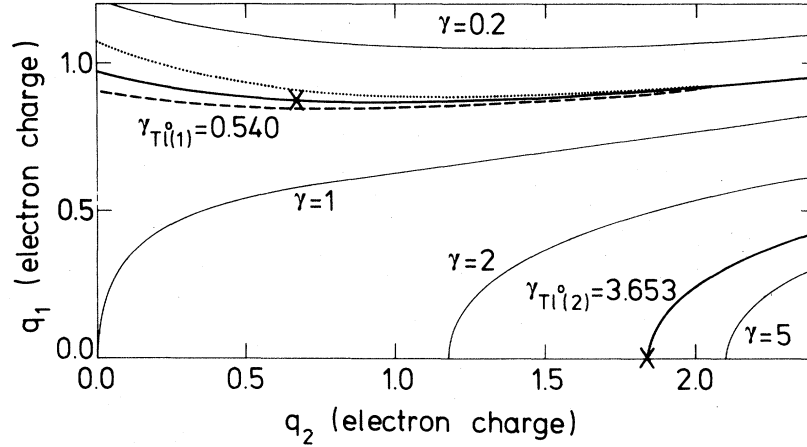


FIG. 6. Set of calculated curves of constant ratio $\gamma = A_{\perp}/A_{\parallel}$ of the hf parameters is shown in a (q_2, q_1) plane, including those corresponding to the experimental hf parameters of $\text{Tl}^0(1)$ and $\text{Tl}^0(2)$, measured at 14 K (Table I). The full lines are calculated for the value of $\alpha = 0.5$, while for $\text{Tl}^0(1)$ curves for $\alpha = 0.25$ (· · ·) and 0.75 (---) are shown. For each of the defects a cross indicates the best fit of the experimental parameters (Table IV).

As a function of q_2 we have drawn in Fig. 7 for each point on the $\gamma = \text{constant}$ curves for $\text{Tl}^0(1)$ and $\text{Tl}^0(2)$ the localization factor f needed to scale the calculated hf parameters to their experimental values. The g factors g_{\parallel} and g_{\perp} are also given as a function of q_2 using the corresponding q_1 value on the appropriate γ curve in Fig. 6, and the resulting f value.

In Fig. 7 the experimental g values of both centers are indicated. For $\text{Tl}^0(1)$ this yields an upper and lower limit for q_2 and from the mean value the best fit as given in Table IV is derived. For $\text{Tl}^0(2)$ it is clear that for the lowest possible q_2 value, $q_2 = 1.84$ (which implies $q_1 = 0$), the calculated g values are closest to the experimental ones and the parameters corresponding to this point are again presented in Table IV.

From this table we can see that the values obtained for the first- and second-degree field charges q_1 and q_2 are in good qualitative and reasonable quantitative agreement with the models presented in Sec. IV. The first-degree field cancels ($q_1 = 0$) for $\text{Tl}^0(2)$ in agreement with the symmetric configuration of the two vacancies ($e_1 = e_2$) and the second-degree field q_2 is much stronger than for the one vacancy $\text{Tl}^0(1)$ center. Furthermore, q_1 and q_2 are comparable to each other for $\text{Tl}^0(1)$ which is also in agreement with the one-vacancy model ($e_2 = 0$). However, the calculated charges in Table IV are reduced to about 70 and 90% of the "ionic" values expected from the one- and two-vacancy models. This is very likely a reflection of the delocalization of the Tl^0 valence electron.

From the localization factors f in Table IV one

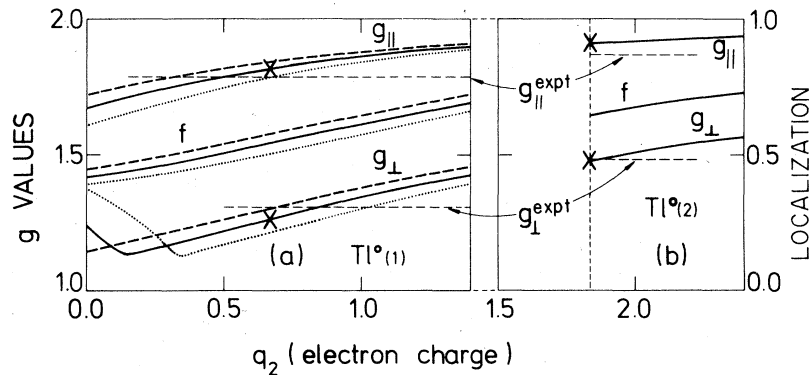


FIG. 7. Plot of the localization fraction f and the g values g_{\perp} and g_{\parallel} corresponding to the points on the $\gamma = A_{\perp}/A_{\parallel} = \text{const}$ curves (see Fig. 6) of (a) the $\text{Tl}^0(1)$ defect ($\gamma = 0.540$), and (b) the $\text{Tl}^0(2)$ defect ($\gamma = 3.653$) as a function of the second-degree charge q_2 . (Full line: $\alpha = 0.5$, dotted and broken line for $\alpha = 0.25$ and 0.75, respectively). The best fits for each defect (Table IV) are indicated by a cross.

TABLE IV. Crystal-field charges q_1 , q_2 , and localization factor f obtained from an exact fit to the $Tl^0(1)$ and $Tl^0(2)$ hyperfine parameters and an approximate fit to the g factors. The estimated value of $\alpha=0.5$ was used in this fitting procedure.

| Center | q_2 | q_1 | f | $g_{ }$ | g_{\perp} |
|----------------|-------|-------|-------|----------|-------------|
| $Tl^0(1)$ calc | 0.678 | 0.870 | 0.544 | 1.820 | 1.265 |
| $Tl^0(1)$ expt | | | | 1.7892 | 1.3077 |
| $Tl^0(2)$ calc | 1.839 | 0 | 0.646 | 1.910 | 1.479 |
| $Tl^0(2)$ expt | | | | 1.8694 | 1.4822 |

deduces that in the case of $Tl^0(2)$ 35% of the valence electron is shared by the two vacancies and the surrounding ions. For $Tl^0(1)$ the delocalization is higher, namely, 45%, despite the fact that only one vacancy is involved.

It is beyond the scope of this work to investigate the precise details of the delocalization: a molecular orbital approach will be needed for this. At this point we only note that our pragmatic atomic approach has provided a reasonable and consistent interpretation of the g and hf data.

G. Qualitative discussion of the ESR linewidths

The linewidths of the ESR spectra of $Tl^0(1)$ and $Tl^0(2)$ very probably result from unresolved shf interaction of the unpaired electron with surrounding Cl^- and K^+ nuclear spins. The electron will spend part of its time in an F -center-type orbital on the vacancies. The linewidth resulting from this can be expressed as a fraction of the F -center linewidth, which is 4.6 mT in KCl.³⁰ Only $\frac{5}{6}$ of this will be taken into account because one of the K^+ ions is replaced by Tl^0 . The attractive field of the negative-ion vacancies induces a deformation of the Tl^0 valence orbital towards a p_z orbital, oriented along the tetragonal axis of the centers. Therefore we expect the interaction of the electron spin with the Cl^- nuclear spins lying in the plane perpendicular to the tetragonal axis to be small. An analogous situation is found for the tetragonal Sn^+ center in KCl (Ref. 7) which is not disturbed by any vacancy. In this case resolved shf structure is found only with the two chlorine nuclei along the $\langle 100 \rangle$ symmetry axis of the center. We will therefore in the $Tl^0(1)$ center take only one Cl^- nuclear spin into account, and none in the $Tl^0(2)$ center.

The shf coupling with the one neighboring Cl^- nucleus along $\langle 100 \rangle$ in $Tl^0(1)$ would yield a four-line structure. However each of these lines has an intrinsic linewidth determined by other factors. Among these is the 45% delocalization obtained from the theory. Supposing this means 45% F -center charac-

ter, one obtains a linewidth of about 1.8 mT, which is more than half the experimental reduced width of 2.7 mT (Table I). Under these circumstances the shf structure cannot be resolved. An estimate of the chlorine shf coupling parameter needed to obtain the experimental linewidth yields 0.75 mT. This is smaller but of the same magnitude as the chlorine shf coupling parameters for the isoelectronic Sn^+ center⁷:

$$A_{\perp}(Cl) = 1.43 \text{ mT} , \quad A_{||}(Cl) = 1.99 \text{ mT} ,$$

In the $Tl^0(2)$ center the shf coupling to the Cl^- nuclei is probably negligible. If the 35% delocalization from the theory is again F -center-like, a linewidth of about 1.3 mT is found which is somewhat larger than the experimental 0.75 mT value given in Table I. These qualitative arguments illustrate however why the ESR linewidth of the $Tl^0(2)$ center is so much smaller than that of the $Tl^0(1)$ center.

VI. PRODUCTION, OPTICAL, AND THERMAL PROPERTIES OF THE Tl^0 CENTERS

A. Some data on the primary $Tl^0(0)$ center

Before describing our experiments it is useful to recall a few facts about the primary $Tl^0(0)$ defect^{1,5,6} whose model is presented in Fig. 2(c). These centers are produced rapidly and efficiently together with some amount of F center by x irradiation of KCl:TlCl at liquid nitrogen temperatures. At the same time a high concentration of $Cl_2^-V_K$ centers (self-trapped hole centers) and a small amount of Tl^{2+} (Refs. 1 and 14) centers are created. The primary $Tl^0(0)$ is formed when a substitutional Tl^+ traps a mobile electron produced by the x irradiation. The V_K centers start hopping above 210 K (Ref. 4) and the holes are trapped by the Tl^+ ions thus strongly enhancing the Tl^{2+} concentration. Around 290 K the $Tl^0(0)$ decay by losing their trapped electron and these in turn destroy a good fraction of the positively charged Tl^{2+} defects. A strong thermoluminescent peak characterizes this process. The optical absorption bands of

$Tl^0(0)$ extend from 300 to 800 nm with two weak additional peaks at 1250 and 1500 nm. Excitation with polarized light produces no optical anisotropy even at 4.2 K.³¹

B. Production of $Tl^0(1)$ and $Tl^0(2)$ by irradiation at various temperatures above 200 K

The $Tl^0(1)$ and $Tl^0(2)$ centers are readily produced in reasonable quantities by x irradiation at room temperature, but they are not formed below 220 K. In order to find the optimum production temperatures the following experiment was performed: At various temperatures between 200 and 320 K a $KCl:Tl^+$ sample was x irradiated for 15 min and the ESR peak intensities of $Tl^0(1)$ and $Tl^0(2)$ were recorded. In order to restore the sample to its initial state it was warmed to 400°C and quenched to room temperature before each irradiation. The solid lines in Fig. 8 show clearly that $Tl^0(1)$ is produced with maximum efficiency at ~260 K while ~280 K is the optimum temperature for $Tl^0(2)$. The relative intensities of $Tl^0(1)$ and $Tl^0(2)$ in this figure are quite arbitrary, but because of its narrow linewidth it is clear that the $Tl^0(2)$ concentration is substantially smaller than the $Tl^0(1)$ one. The data presented in Fig. 8 are consistent with the $Tl^0(1)$ and $Tl^0(2)$ models set forth in Fig. 2. Indeed, because $Tl^0(2)$ involves one more negative-ion vacancy than $Tl^0(1)$ a reasonable concentration of the latter [or its precursor under elec-

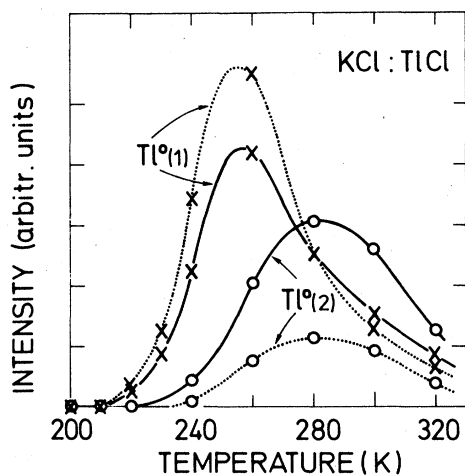


FIG. 8. Isochronal (15 min) production of the $Tl^0(1)$ and $Tl^0(2)$ centers (\times and \circ , respectively), by x irradiation of $KCl:TlCl$ at temperatures between 200 and 320 K (full lines). A subsequent F bleach in the ESR cavity (5 min) yields new intensities represented by a broken line. Before each x irradiation thermal annealing to 400°C was applied to the crystal.

tron trapping which we will indicate by $Tl^+(1)$] must have been formed before a measurable concentration of $Tl^0(2)$ can be produced. The lower production efficiency of both Tl^0 defects above 280 K may be attributed to further electron and negative-ion vacancy trapping and to the fact that at 290 K the primary $Tl^0(0)$ defect is not thermally stable. The $Tl^+(1)$ center is a substitutional Tl^+ ion next to a negative-ion vacancy. The evidence to be presented in Sec. VIE indicates that, $Tl^+(1)$, the precursor center of $Tl^0(1)$ under electron trapping, also decays thermally around 280 K. This will necessarily adversely affect the production of both $Tl^0(1)$ and $Tl^0(2)$ above 280 K in agreement with the high-temperature results in Fig. 8.

C. Production by x rays at 260 K as a function of time

In the following experiment the production of $Tl^0(1)$, $Tl^0(2)$, and Tl^{2+} was studied by ESR as a function of x-irradiation time at 260 K. This temperature was chosen because (i) both $Tl^0(1)$ and $Tl^0(2)$ are efficiently produced (see Fig. 8), (ii) the primary $Tl^0(0)$ is still thermally stable at this temperature ($T_{\text{decay}} = 290$ K), and (iii) the V_K centers are not stable ($T_{\text{decay}} = 210$ K), making that most mobile holes produced by the irradiation are trapped by Tl^+ ions and form Tl^{2+} . The results are plotted in Fig. 9. The rate of formation of Tl^{2+} is very high at the beginning of the irradiation, but it drops off rapidly after about 5 min. The $Tl^0(0)$ ESR spectrum is unobservable, but the initial stage of production is expected to be similar to that of Tl^{2+} . The $Tl^0(1)$ and $Tl^0(2)$ centers have a much slower rate of formation, the $Tl^0(2)$ rate being the slowest.

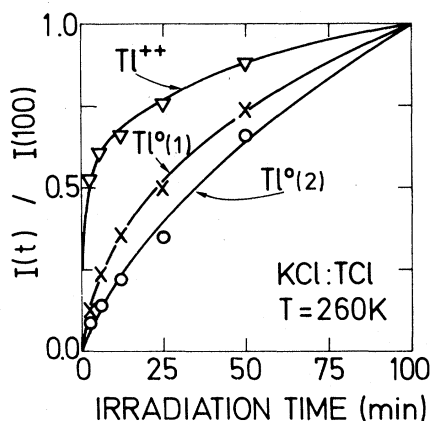


FIG. 9. Isothermal ($T = 260$ K) production measurement of the $Tl^0(1)$, $Tl^0(2)$, and Tl^{2+} defects (\times , \circ , and ∇ , respectively), in $KCl:TlCl$, as a function of time of x irradiation. The intensities are normalized to the value obtained after 100 min of irradiation.

These observations are readily explained. The rapid initial rate for Tl^{2+} formation underscores the fact that the x irradiation produces efficiently large quantities of mobile holes and electrons which are quickly stabilized as Tl^{2+} and primary $Tl^0(0)$ defects, respectively. The creation of $Tl^0(1)$ and $Tl^0(2)$ requires (i) the existence of a reasonable $Tl^0(0)$ concentration, and (ii) the availability of negative-ion vacancies (which are known to be mobile at 260 K). The creation of negative-ion vacancies implies the creation of halogen interstitials. The production of the latter, and consequently of the negative-ion vacancies, is known to be much less efficient compared to the production of electrons and holes. In fact, in order to produce interstitial concentrations comparable to trapped electron or hole center concentrations one needs x-irradiation times which are roughly one order of magnitude longer. In view of these considerations the much slower rates of formation of $Tl^0(1)$ and $Tl^0(2)$ compared to Tl^{2+} are quite understandable and lend general support to the defect models proposed in Fig. 2. The lower production rate of $Tl^0(2)$ is again in agreement with the assumption that two negative-ion vacancies are present in the structure.

D. Pulse annealing experiments

1. Production of $Tl^0(1)$ and $Tl^0(2)$ by vacancy stabilization

In this experiment we wanted to separate the processes dependent upon the production and mobility of electrons and holes from those dependent on the migration of negative-ion vacancies. To this end a KCl:TlCl sample was x irradiated for 20 min at 200 K. This irradiation produces a large amount of trapped electron centers (mostly the primary $Tl^0(0)$ defect and F centers), trapped hole centers (mostly the $Cl_2^- V_K$ center) and an amount of negative-ion vacancies which are immobile (they start to migrate above ~ 230 K). Then the sample was pulse annealed (5 min at each temperature, 10 K apart) to room temperature. The V_K centers, or the holes for that matter, become mobile at 210 K (Ref. 4), and are retrapped mostly by Tl^+ ions forming Tl^{2+} centers. Indeed, at the doping levels we are using the Tl^+ concentrations still far outweighs the $Tl^0(0)$ one. This hole retrapping process, is complete by the time 230 K is reached where $Tl^0(1)$ and $Tl^0(2)$ start to form (Fig. 10). Both continue to increase when the temperature is raised further, very likely we believe, because the now mobile negative-ion vacancies are trapped by the primary $Tl^0(0)$ centers. Above 270 K the $Tl^0(2)$ decays strongly while $Tl^0(1)$ shows only a small drop. We note that these changes coincide with the known decay temperature 290 K of the primary $Tl^0(0)$ center^{1,32} and consequently we propose the following explanation.

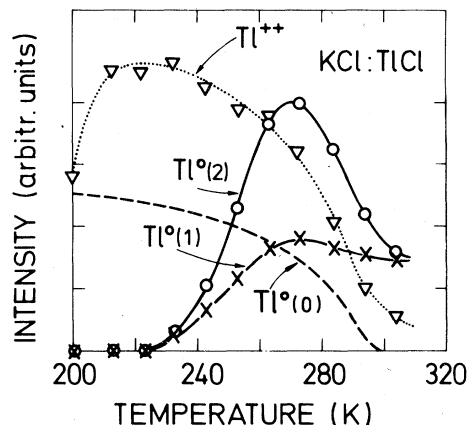


FIG. 10. Intensities of the $Tl^0(1)$, $Tl^0(2)$, and Tl^{2+} ESR spectra (\times , \circ , and ∇ , respectively), obtained after a 20-min x irradiation of KCl:TlCl at 200 K, are displayed as a function of the temperature corresponding to consecutive pulse annealings of 5 min. The pulse-anneal data of Delbecq *et al.* (Ref. 32) concerning the decay of $Tl^0(0)$ are also given.

In forming $Tl^0(1)$ and $Tl^0(2)$ not all the primary $Tl^0(0)$ have been used up (maybe the vacancies are, maybe not). These $Tl^0(0)$ decay thermally around 290 K releasing mobile electrons which are in turn strongly attracted by the positively charged $Tl^0(2)$ centers transforming them into Tl^- -type centers. The latter are unobservable in ESR. The $Tl^0(1)$ center, which according to our model is electrically neutral, does not strongly attract mobile electrons. This explains their relative indifference to them. We note again that the proposed $Tl^0(1)$ and $Tl^0(2)$ models in Fig. 2 are naturally consistent with the experimental data.

If the above explanation is correct, one must conclude that the precursor center $Tl^+(1)$ [Fig. 2(d)] of $Tl^0(1)$, is not stable above 270 K. Indeed, such a precursor center is positively charged and would strongly attract the mobile electrons. This would lead to an increase of the $Tl^0(1)$ concentration above 270 K, which is not observed. In Sec. VI E we shall in fact present evidence that the $Tl^+(1)$ precursor center can be produced below 270 K but that it decays above this temperature.

2. Pulse anneal after x irradiation at RT: Thermal stability of the Tl^0 defects

In order to measure the thermal decay of the $Tl^0(1)$ and $Tl^0(2)$ centers a KCl:TlCl crystal was x irradiated at RT during 30 min and the ESR spectra were measured after each of a series of pulse-anneal treatments of 5 min about 15 K apart. As is shown in Fig. 11 the intensity of $Tl^0(2)$, and to a lesser ex-

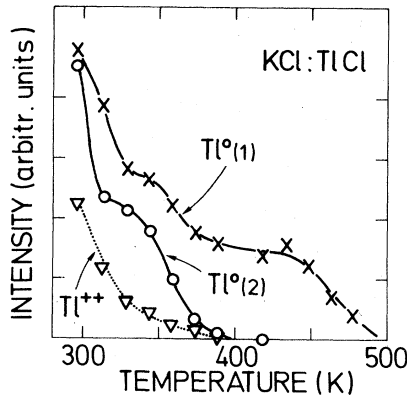


FIG. 11. Pulse-anneal data concerning the decay of the $Tl^{0(1)}$, $Tl^{0(2)}$, and Tl^{2+} defects (\times , \circ , and ∇ , respectively), in a KCl:TlCl crystal which was x irradiated for 40 min at RT.

tent the one of $Tl^{0(1)}$, drop fast after the first annealing step at 313 K. At the same time the Tl^{2+} centers show a strong decay, which is a result of trapping of the electrons released by the $Tl^{0(0)}$ defects. Indeed, the latter centers are decaying around RT.^{1,32} The decay of the $Tl^{0(2)}$ centers is comparable to that obtained in the same temperature range in the foregoing annealing experiment (see Fig. 10). The $Tl^{0(1)}$ decay is much stronger than in the previous experiment. The quantitative differences between the two experiments are quite understandable in view of the very different conditions of production of the defects. In the present experiment the x irradiation was performed at a temperature at which the primary $Tl^{0(0)}$ centers are becoming unstable. The initial decay of the $Tl^{0(1)}$ and $Tl^{0(2)}$ centers probably results from this situation. From the further annealing data one can see that both $Tl^{0(1)}$ and $Tl^{0(2)}$ centers are stable above 313 K.

The $Tl^{0(2)}$ defects start decaying around 360 K, and have disappeared completely at 390 K. One notes from Fig. 11 that this decay occurs simultaneously with the disappearance of the Tl^{2+} centers. It is possible that the $Tl^{0(2)}$ defects are destroyed by trapping of holes released by the Tl^{2+} centers.

The $Tl^{0(1)}$ centers are much more stable and decay around 460 K. After a pulse anneal to a temperature in the region of decay of $Tl^{0(1)}$, the crystal is losing the color obtained by the x irradiation, which shows that the F centers are also annealed out. This points to a release of interstitial ions or atoms from traps in the crystal. For $Tl^{0(1)}$, and as mentioned above also for $Tl^{0(2)}$, it is not certain that the decay of the defect is a result of its thermal instability: secondary processes—in the $Tl^{0(1)}$ case the decay of interstitial defects—may be involved.

E. Behavior under optical excitation of F centers

The foregoing experiments have shown that (i) the $Tl^{0(2)}$ center exerts a strong attraction for mobile electrons, and (ii) that $Tl^{0(1)}$ does not. Furthermore the possibility was raised of the existence of the precursor center under electron trapping of the $Tl^{0(1)}$ center, i.e., the $Tl^{+(1)}$ center. In order to investigate these points further the behavior of the ESR spectra under optical F -center excitation was studied, because such an excitation produces mobile electrons in the crystal.

1. F -center excitation at 10 K after x irradiation between 200 K and RT

The experiment of Fig. 8 was repeated but with an important addition, i.e., after the x irradiation of 15 min at the chosen temperature and after the $Tl^{0(1)}$ and $Tl^{0(2)}$ ESR intensities were recorded (solid lines of Fig. 8), the sample was optically excited *in situ* in the F band at 10 K for several minutes. The new ESR intensities were then recorded at 10 K after which the crystal was heated to $\sim 400^\circ\text{C}$ in order to prepare it for the next x irradiation at a 10-K higher temperature.

The results of such optical F -center bleaching at 10 K are presented in Fig. 8 as dotted lines. It is seen that at all temperatures the $Tl^{0(2)}$ intensity drops considerably under F illumination. This behavior is in agreement with the proposed two vacancy model of $Tl^{0(2)}$ (Fig. 2) which is expected to exert a strong Coulomb attraction on electrons. The resulting Tl^- -like center is unobservable in ESR. However, it is also conceivable that the $Tl^{0(2)}$ destruction is caused by direct optical excitation into a $Tl^{0(2)}$ optical-absorption band which more or less overlaps the F -center absorption at 540 nm. Indeed, a preliminary optical investigation has shown that in x -irradiated KCl: Tl^+ crystal a band is present around 555 nm. A correlation with the $Tl^{0(2)}$ center could not yet be readily proven or disproven (see Sec. VIF).

The $Tl^{0(1)}$ intensity obtained by x irradiation below 270 K is increased substantially after a subsequent optical F -center excitation at 10 K. This represents strong evidence that below 270 K the $Tl^{+(1)}$ precursor center is produced. This $Tl^{+(1)}$ precursor, formed during the x irradiation when a mobile negative-ion vacancy is trapped next to a substitutional Tl^+ , is positively charged and thus strongly attracts mobile electrons. This strong attraction permits $Tl^{+(1)}$ to overcome its numerical disadvantage in comparison with the neutral substitutional Tl^+ ions with which it is competing for electrons below 270 K.

Above 270 K, e.g., at room temperature, there is no $Tl^{0(1)}$ increase under F -center illumination; in

fact a small decrease is observed. We conclude, in agreement with the conclusions of Sec. VID, that the $Tl^{+}(1)$ precursor center is not thermally stable above 270 K. Consequently there are no $Tl^{+}(1)$ precursor centers to trap electrons and enhance the $Tl^{0}(1)$ concentration. The observed small decrease of $Tl^{0}(1)$ may be caused by electron trapping [forming a $Tl^{-}(1)$ -like center, unobservable with ESR] or by direct optical excitation into some $Tl^{0}(1)$ optical absorption band. The latter could not be ascertained in the preliminary optical-absorption experiment.

2. *F* bleach consecutive to *x* irradiation at 200 K and pulse anneal to 240 K

The existence of the $Tl^{+}(1)$ defect, precursor under electron trapping of the $Tl^{0}(1)$ defect, is strongly supported by the results of the following experiment. After 30 min of *x* irradiation at 200 K, a KCl:TlCl crystal was pulse annealed for 10 min at 240 K, i.e., above the temperature at which the anion vacancies are becoming mobile.¹² As a result $Tl^{0}(1)$ and $Tl^{0}(2)$ ESR signals were produced, in the same way as described in Sec. VID during the simple pulse-anneal experiments. After the annealing at 240 K an *in situ* optical excitation in the *F* band ($T \approx 40$ K) resulted in a more than fourfold increase of the $Tl^{0}(1)$ concentration, and reduces the $Tl^{0}(2)$ signals to below the detection limit.

It is worth pointing out that very different processes can occur by this treatment, compared to an *F* bleach after *x* irradiation of the sample at 240 K (Fig. 8). By the *x* irradiation at 240 K free electrons (and holes) as well as mobile anion vacancies are produced simultaneously. On the contrary, in the present experiment electrons are freed by the *x* irradiation at 200 K, while the motion of the anion vacancies, also produced by the *x* irradiation, is frozen: no migration of the vacancies towards a $Tl^{0}(0)$ or a Tl^{+} center can occur. In the pulse-annealing step the vacancy migration is allowed, while none or very few mobile electrons are produced. Tl^{+} and $Tl^{0}(0)$ are competing traps for these anion vacancies, yielding the $Tl^{+}(1)$ and $Tl^{0}(1)$ defects, respectively. The Tl^{+} center possesses a higher concentration than the $Tl^{0}(0)$ center, but the latter carries an effectively negative charge which exerts a Coulomb attraction on the anion vacancies. The low-temperature *F* bleach will free electrons which can be trapped by the positively charged $Tl^{+}(1)$ centers, forming the $Tl^{0}(1)$ centers. From the drastic enhancement of the $Tl^{0}(1)$ concentration by the *F* bleach it is concluded that at least three times as much anion vacancies had been trapped at Tl^{+} than at $Tl^{0}(0)$ centers during the pulse anneal at 240 K.

In Fig. 1(d) the simplest structure for the $Tl^{+}(1)$ defect is given. If another configuration is taken into

consideration it is necessary to assume a jump of the negative-ion vacancy from a neighboring position to the NN position of the Tl^{0} atom during the electron capture process, in order to obtain the model of $Tl^{0}(1)$ [Fig. 2(a)].

One should take into account that two other processes can influence the experiment presented here. First it is possible that part, or all, of the $Tl^{0}(1)$ defects produced during the pulse annealing at 240 K, do not result from vacancy trapping near $Tl^{0}(0)$ centers, but from electron capture at the $Tl^{+}(1)$ defects. A small amount of mobile electrons can be produced by the thermal decay of some electron trapping centers such as, the F' center. Second one should remember that the V_K center becomes mobile around 210 K and some of the holes could be trapped by $Tl^{0}(1)$ defects, which is an indirect way to produce the $Tl^{+}(1)$ defect.

The total decay of the $Tl^{0}(2)$ ESR signal by the low-temperature *F* bleach can be explained, as was also mentioned before in Sec. VI, by trapping of a second electron, yielding a Tl^{-} -type defect. The latter is, however, not detected in ESR. Alternatively, we suggested a direct optical excitation in an absorption band of the $Tl^{0}(2)$ center which would overlap with the *F* band.

3. *F*-center excitation at room temperature

In this experiment a KCl: Tl^{+} sample was optically excited in the *F* band at room temperature after the crystal had been *x* irradiated at room temperature for about 15 min (Fig. 12).

The $Tl^{0}(1)$ intensity typically doubles within a few minutes of *F*-center excitation after which it quickly reaches a saturation level. We concluded already in

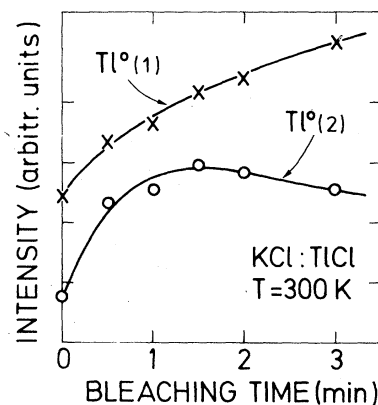


FIG. 12. Intensities of the $Tl^{0}(1)$ and $Tl^{0}(2)$ defects (\times and O , respectively), after 30 min of *x* irradiation at RT as a function of time of subsequent *F* bleaching at RT.

Secs. VID and VIE that no $Tl^{+}(1)$ precursor centers are produced by x irradiation at room temperature. Thus the observed $Tl^{0}(1)$ increase cannot be attributed to electron trapping by $Tl^{+}(1)$. Rather, it should be remembered that optical excitation of F centers at room temperature yields both mobile electrons and mobile negative-ion vacancies whose motions may or may not be correlated. Thus the strong $Tl^{0}(1)$ increase is ascribed to trapping by a substitutional Tl^{+} ion of a mobile negative-ion vacancy and a mobile electron either simultaneously or in very rapid succession.

The effect of optical F -center excitation at room temperature on the $Tl^{0}(2)$ center is the following: A strong increase (typically a quadrupling) of the $Tl^{0}(2)$ intensities after a few minutes of illumination followed by a slow decrease. The explanation is basically the same as for $Tl^{0}(1)$: A substitutional Tl^{+} impurity ion catches in rapid succession two mobile negative-ion vacancies and one mobile electron. The observed slow decrease after a few minutes may be caused either by trapping of a second electron or by direct excitation into a $Tl^{0}(2)$ optical-absorption band. Again the proposed models of $Tl^{0}(1)$ and $Tl^{0}(2)$ are naturally consistent with the experimental observations and their explanation in terms of the known mobility of electrons and negative-ion vacancies.

F. Optical absorption experiments

The electron and hole trapping properties of Tl^{+} impurities in KCl have been studied by optical-absorption and thermoluminescence measurements.¹ After γ irradiation at 77 K the absorption bands attributed to the trapped electron center, $Tl^{0}(0)$ (at 380, 640, 1260, and 1500 nm), and to the trapped hole center, Tl^{2+} (at 220, 262, 294, and 364 nm), were measured. Recently³³ the creation of an absorp-

tion band at 278 nm in KCl:TlCl by x irradiation at 300 K was attributed to trapping of electrons at a thallium defect. The latter was concluded from the growth of this band under an optical F -center bleach at low temperature.

In crystals containing a higher concentration of TlCl (about 0.25 mol%) some of the Tl^{+} ions are paired, and after a low-temperature x irradiation it was possible to measure the absorption bands (at 233, 460, 860, and 1760 nm) of the trapped electron defect Tl_2^{+} .³² More recently,³⁴ very strongly doped crystals (up to 2 mol%) were studied after x-ray treatment at 77 K. From ESR measurements it was determined that Tl_2^{3+} -type defects were produced, probably close to a Tl^{0} center. It was also claimed that Tl_2^{+} and Tl^{2+} defects were paired in these crystals.

Several optical studies report the production of Tl^{-} -type defects by additive coloring of KCl:TlCl crystals,³⁵ or else by electrolytic coloring of KCl:(TlCl + $CaCl_2$) and KCl:(TlCl + $SrCl_2$).³⁶

An attempt was made to identify the optical-absorption bands corresponding to the $Tl^{0}(1)$ and $Tl^{0}(2)$ defects, discussed in this paper. Figure 13(a) shows the optical-absorption spectrum at 77 K of a KCl:TlCl crystal after x irradiation at RT for 30 min. The spectrum exhibits the characteristic F and K bands (539 and 455 nm, respectively), as well as the bands of Tl^{+} (209 and 247 nm) and Tl^{2+} . No $Tl^{0}(0)$ defects are produced at this temperature.^{1,33} Several broad absorption bands of low intensity can also be distinguished around 278 nm, between 320 and 380 nm, and at 625 nm. By doing consecutive F bleachings at RT the intensity of the bands of the F and the Tl^{2+} centers decrease continuously [Figs. 13(b), 13(c), and 13(d)]. An apparent shift of the F band occurs from 539 to 552 nm, which indicates the presence of an additional absorption band around 555 nm. During the F bleach new bands can be distinguished at 318, 378, 425, 460, 625, and 845 nm.

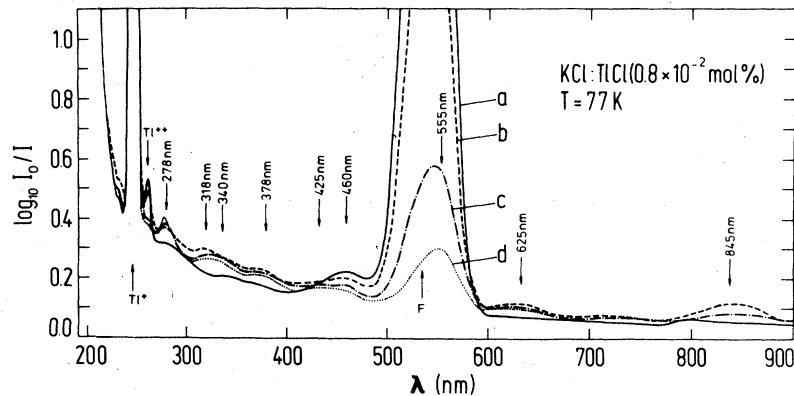


FIG. 13. Optical-absorption spectra of a KCl:TlCl crystal (concentration 0.8×10^{-2} mol%) (a) after 30 min of x irradiation at RT, followed by a F bleach at RT lasting (b) 45 s, (c) 5 min, and (d) 13 min.

Except for the latter two all of these bands increase continuously, reaching a saturation level after several minutes of bleaching. The bands at 625 and at 845 nm reach a maximum height after a few minutes, and decrease afterwards to saturation levels of about 50% and 30%, respectively, of their maximum values. The absorption at 318 nm is broadened toward longer wavelength, indicating that another band around 340 nm should be considered.

KCl crystals with a lower content of TlCl (less than 10^{-4} mol%) were submitted to the same treatment: x irradiation at RT followed by F bleaching at RT. No ESR signals of thallium-type defects could be observed, and the optical-absorption spectra exhibit quite different patterns [Figs. 14(a), 14(b), and 14(c)]. After the x irradiation, besides the Ti^+ and the F bands, the absorption bands of the M , R_1 , and R_2 centers are clearly visible. By illumination in the F band the intensity of all these bands decreases continuously and three bands at 278, 378, and 460 nm can be distinguished with intensities comparable to those found in the KCl:TlCl crystals with a higher doping level. This experiment proves that the absorption bands at 278, 376, and 460 nm cannot be attributed to the Ti^0 defects detected in ESR. It was checked that the remaining absorption bands do not belong to the Ti_2^+ center, which possesses bands at 460, 860, and 1760 nm among which the latter one is the most intense. No absorption could be detected in the 1760-nm region.

Selective bleaching experiments with polarized light were performed at low temperature inside the ESR cavity. Samples of the usual TlCl concentration were x irradiated for 30 min and F bleached for 10 min at RT. By this treatment only small amounts of Ti^{2+} and F centers remain. The ESR spectra were measured with $\vec{H} \parallel \langle 100 \rangle$ before and after an illumination of the sample inside the ESR cavity at $T = 30$ K, with

light polarized parallel to the magnetic field, at wavelengths corresponding to the unidentified absorption bands. A third ESR spectrum was recorded after a reorientation of the crystal with the other $\langle 100 \rangle$ direction along the static field. From these measurements a selective bleaching of a given orientation or a reorientation, of the $\text{Ti}^0(1)$ and $\text{Ti}^0(2)$ centers could be detected.

Changes in the number of Ti^0 centers resulted from illuminating at 318 nm [$\text{Ti}^0(1)$ diminishes, $\text{Ti}^0(2)$ increases], at 340 nm [$\text{Ti}^0(1)$ diminishes, $\text{Ti}^0(2)$ does not change], at 425 and 845 nm [both $\text{Ti}^0(1)$ and $\text{Ti}^0(2)$ increase] and at 555 and 625 nm [$\text{Ti}^0(1)$ does not change, $\text{Ti}^0(2)$ diminishes]. In general isotropic changes in the intensity of corresponding signals were observed. Only by illuminating at 340 nm a stronger bleaching in the perpendicular component of $\text{Ti}^0(1)$ ESR spectrum was detected. From the above results we tentatively assign the 340-nm band to $\text{Ti}^0(1)$ centers, the 555 and 625-nm band to $\text{Ti}^0(2)$ centers, while the 318-, 425-, and 845-nm bands should be related to other electron trapped centers. From these bleaching experiments one is tempted to relate the 318-nm band to the $\text{Ti}^0(1)$ center. However, another experiment described below contradicts this assignment. Presumably the broad optical absorption of $\text{Ti}^0(1)$ at 340 nm is responsible for the bleaching effect observed at 318 nm. The increase in the number of both $\text{Ti}^0(1)$ and $\text{Ti}^0(2)$ defects by bleaching at 425 and 845 nm could be explained by trapping at the precursor centers of these defects of electrons released from the unknown defects. Such a precursor center, namely, $\text{Ti}^+(1)$, was shown to exist for the $\text{Ti}^0(1)$ defect in Sec. VI E. Alternatively a Ti^- -type defect could be bleached, which through the release of an electron would be converted to a $\text{Ti}^0(1)$ or $\text{Ti}^0(2)$ defect. It should be mentioned that even through long bleachings, only

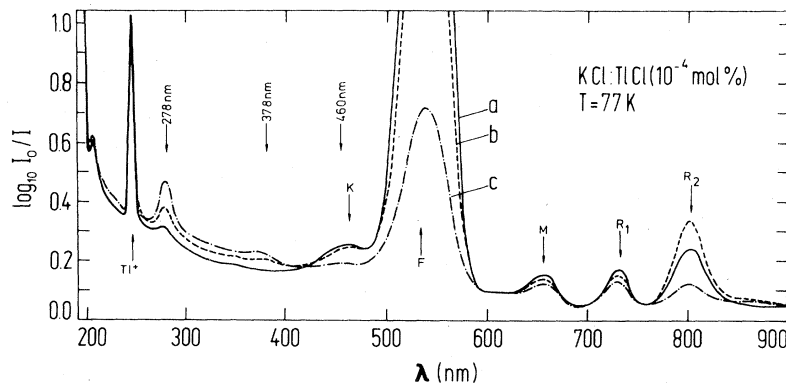


FIG. 14. Optical-absorption spectra of a low concentration ($\leq 10^{-4}$ mol%) KCl:TlCl crystal (a) after 20 min of x irradiation at RT, followed by an F bleach at RT lasting (b) 15 s, and (c) 5 min.

relative changes of intensity of the ESR signals of less than 20% were obtained for any bleaching wavelength.

The following experiments were performed to check the correlation between the height of the new absorption bands and the ESR intensities of the Tl^0 spectra. A KCl:TlCl crystal was x irradiated during 30 min at 200 K, subsequently warmed up to 240 K for 5 min, cooled down to 77 K and bleached for 15 min in the F band. As described earlier (Sec. VI E 2), $Tl^0(2)$ ESR spectra are obtained after pulse annealing to 240 K, but disappear completely during the F bleach at 77 K. It was indeed found that the 625-nm band, which we assigned to $Tl^0(2)$, was absent from the final optical absorption spectrum. (No check could be done for the 555-nm band because it was hidden under a huge F band.) The second experiment was performed both in ESR and in optical absorption. After a 30-min x irradiation at 77 K [no $Tl^0(1)$ or $Tl^0(2)$ signals in ESR] the crystal is warmed up to RT for 5 min [$Tl^0(1)$ ESR spectra have appeared, no $Tl^0(2)$], and finally F bleached at RT for 30 min [the ESR spectra of $Tl^0(1)$ decrease slightly and those of $Tl^0(2)$ become quite intense]. The 625-nm absorption band appears only after the F bleach, together with the $Tl^0(2)$ signals. However, the 318-nm band, which from the bleaching experiments could be related to $Tl^0(1)$, disappears completely during the F bleach at RT, and is not correlated with the ESR signals of the defect.

VII. SUMMARY AND CONCLUSIONS

Two thallium atom-type defects called $Tl^0(1)$ and $Tl^0(2)$, both possessing tetragonal symmetry around $\langle 100 \rangle$ have been discussed in this paper. They are produced in KCl:TlCl crystals by x irradiation at or just below room temperature where negative-ion vacancies (also produced by the irradiation) are known to be mobile. Extensive ESR data concerning the g components, the hf components, and the linewidths are presented and a detailed theoretical analysis of these data is given. This theoretical analysis, based on a relativistic many-body calculation of the Tl^0 atom, is particularly useful for the interpretation of the hf data. Indeed, although the hf tensors of the two Tl^0 defects are comparable in magnitude to one another, the qualitative features of the hf components are quite different. This difference is quantitatively explained by (i) incorporating a tetragonal crystal field into the atomic calculation, and (ii) by introducing a 35 to 45% delocalization of the $6p$ Tl^0 electron towards the ions immediately surrounding

the Tl^0 atom. The charges producing the tetragonal fields are found to be positive for both defects strongly pointing to one or more negative-ion vacancies as being responsible for the field. Furthermore, the analysis shows that for a description of the $Tl^0(1)$ hf data a single positive charge is required, while for $Tl^0(2)$ two symmetrically placed positive charges are needed. As a result it is proposed that in the $Tl^0(1)$ model a Tl^0 atom on a positive-ion site is associated with one nearest-neighbor negative-ion vacancy along $\langle 100 \rangle$ and that in the $Tl^0(2)$ model the Tl^0 is flanked by two-nearest-neighbor negative-ion vacancies along $\langle 100 \rangle$. These models are fully confirmed by extensive x-ray production data, thermal anneal data, and optical-excitation experiments. The latter experiments also provide convincing evidence for the existence of a $Tl^+(1)$ defect consisting of a substitutional Tl^+ ion associated with a single nearest-neighbor negative-ion vacancy. This $Tl^+(1)$ center is the precursor center under electron trapping of the $Tl^0(1)$ defect. Because it is diamagnetic it is not observable in regular ground-state ESR experiments.

Criticism may be leveled against the *ad hoc* manner of introducing delocalization of the $6p$ electron because it is not self-evident that all the calculated contributions to the hf interaction scale with the localization factor. Nevertheless, this pragmatic approach clearly works quite well in explaining the ESR data and consequently the procedure finds its justification in this agreement.

Finally, the exploratory optical-absorption investigation has yielded a complex richness of optical-absorption bands. The correlation of some of these bands with the thallium defects described in this paper will require further detailed study.

ACKNOWLEDGMENTS

The authors would like to thank F. Van Steen and W. Van Puymbroeck for extensive discussions and one of them (W.V.P.) also for rechecking the formula of the atomic calculation. They also thank A. Bouwen for expert experimental support, C. J. Delbecq, P. H. Yuster, and S. Kapphan, for providing some of the KCl:TlCl crystals, and I. Ursu for his kind cooperation. One of us (E.G.) thanks the IWONL (Instituut voor Wetenschappelijk Onderzoek in Nijverheid en Landbouw) for a scholarship. Financial support of the IKW (Interuniversitair Instituut voor Kernwetenschappen) is gratefully acknowledged. This work was performed within the framework of a Belgian-Roumanian scientific cooperative research project.

- ¹C. J. Delbecq, A. K. Gosh, and P. H. Yuster, *Phys. Rev.* **151**, 599 (1966).
- ²C. J. Delbecq, B. Smaller, and P. H. Yuster, *Phys. Rev.* **111**, 1235 (1958); C. J. Delbecq, W. Hayes, and P. H. Yuster, *ibid.* **121**, 1043 (1961).
- ³T. O. Woodruff and W. Känzig, *J. Phys. Chem. Solids* **5**, 268 (1958).
- ⁴D. Schoemaker, *Phys. Rev. B* **7**, 786 (1973).
- ⁵C. J. Delbecq, A. K. Gosh, and P. H. Yuster, *Phys. Rev.* **154**, 797 (1967).
- ⁶C. J. Delbecq, Y. Toyozawa, and P. H. Yuster, *Phys. Rev. B* **9**, 4497 (1974).
- ⁷C. J. Delbecq, R. Hartford, D. Schoemaker, and P. H. Yuster, *Phys. Rev. B* **13**, 3631 (1976).
- ⁸W. Van Puymbroeck, J. Andriessen, and D. Schoemaker, in *Proceedings of the 1980 Conference of the Condensed Matter Division of the European Physical Society*, Antwerp, 1980 (unpublished), p. 69.
- ⁹P. G. Baranov and V. A. Khramtsov, *Fiz. Tverd. Tela* **21**, 1455 (1979) [*Sov. Phys. Solid State* **21**, 839 (1979)].
- ¹⁰E. Goovaerts, A. Lagendijk, and D. Schoemaker, in *Proceedings of the International Conference on Defects in Insulating Crystals*, Gatlinburg, 1977 (unpublished), p. 153.
- ¹¹D. Schoemaker, E. Goovaerts, and S. V. Nistor, *Bull. Am. Phys. Soc.* **23**, 200 (1978).
- ¹²F. Van Steen and D. Schoemaker, *Phys. Rev. B* **19**, 55 (1979).
- ¹³*American Institute of Physics Handbook*, 3rd ed. (McGraw-Hill, New York, 1972), pp. 8–73.
- ¹⁴D. Dreybrodt and D. Silber, *Phys. Status Solidi* **20**, 337 (1967); W. Frey, R. Huss, H. Seidel, and E. Werkmann, *Phys. Status Solidi (b)* **68**, 257 (1975).
- ¹⁵From atomic data [Landolt-Börnstein, *Teil Atome und Ionen* (Springer, Berlin, 1950), Vol. 1] or from the energy difference $\epsilon_{1/2} - \epsilon_{3/2}$ as calculated in Eq. (32) of Sec. V F of this paper.
- ¹⁶J. Andriessen, D. Van Ormondt, S. N. Ray, and T. P. Das, *J. Phys. B* **11**, 2601 (1978).
- ¹⁷J. Andriessen, S. N. Ray, T. Lee, T. P. Das, and D. Ikenberry, *Phys. Rev. A* **13**, 1669 (1976).
- ¹⁸J. Andriessen, K. Raghunathan, S. N. Ray, and T. P. Das, *Phys. Rev. B* **15**, 2533 (1977).
- ¹⁹Mina Vajed-Samii, S. N. Ray, and T. P. Das, *Phys. Rev. A* **20**, 1787 (1979).
- ²⁰M. A. Coulthard, University of Melbourne Internal Report No. HM-P-66/4 (unpublished).
- ²¹H. P. Kelly, *Adv. Theor. Phys.* **2**, 75 (1968).
- ²²G. Gould, *Phys. Rev.* **101**, 1828 (1956).
- ²³C. J. Schuler, M. Ciftan, L. C. Bradley, and H. H. Stroke, *J. Opt. Soc. Am.* **52**, 501 (1962); A. Lurio and A. G. Prodel, *Phys. Rev.* **101**, 79 (1956).
- ²⁴E. Fermi and E. Segré, *Z. Phys.* **82**, 729 (1933).
- ²⁵S. N. Ray, J. Andriessen, and T. P. Das, *Bull. Am. Phys. Soc.* **23**, 287 (1978); S. N. Ray, T. P. Das, and J. Andriessen, *ibid.* **24**, 476 (1979).
- ²⁶O. P. Sushkov, V. V. Flambaum, and I. B. Khriplovich, *Opt. Spectrosc. (USSR)* **44**, 2 (1978) [*Opt. Spektrosk.* **44**, 3 (1978)].
- ²⁷J. P. Desclaux and N. Bessis, *Phys. Rev. A* **2**, 1623 (1970).
- ²⁸A. R. Edmonds, *Angular Momentum in Quantum Mechanics* (Princeton University Press, New Jersey, 1960).
- ²⁹J. H. Ammeter and D. C. Schlosnagle, *J. Chem. Phys.* **59**, 4784 (1973).
- ³⁰J. J. Markham, in *Solid State Physics*, edited by F. Seitz and D. Turnbull (Academic, New York 1970), Suppl. 8.
- ³¹C. J. Delbecq and P. H. Yuster (private communication).
- ³²C. J. Delbecq, E. Hutchinson, and P. H. Yuster, *J. Phys. Soc. Jpn.* **36**, 913 (1974).
- ³³T. Tsuboi, *Can. J. Phys.* **57**, 1510 (1979).
- ³⁴Y. Toyotomi and R. Onaka, *J. Phys. Soc. Jpn.* **46**, 1861, 1869 (1979).
- ³⁵L. Ben-Dor, A. Glasner, and A. Zudkevitz, *J. Electrochem. Soc.* **117**, 665 (1970).
- ³⁶A. Ioan and V. Topa, *Rev. Roum. Phys.* **22**, 691 (1977); A. Ioan, V. Topa, and M. Giurgea, *Phys. Status Solidi (b)* **89**, 513 (1978).